Ultra-Slow Orbital and Spin Dynamics in an Electrically Tunable Quantum Dot Molecule

Christopher Thalacker,[1,*] Michelle Lienhart,[1] Markus Stöcker,[1] Nadeem Akhlaq,[1] Irina Ivanova,[1] Nikolai Bart,[2] Arne Ludwig,[2] Johannes Schall,[3] Stephan Reitzenstein,[3] Dirk Reuter,[4] Steffen Wilksen,[5] Christopher Gies,[5] Krzysztof Gawarecki,[6] Paweł Machnikowski,[6] Kai Müller,[7] and Jonathan Finley[1]

[1]*Walter-Schottky-Institute, Technische Universität München, Am Coulombwall 4, 85748 Garching, Germany*
[2]*Faculty of Physics and Astronomy, Ruhr-Universität Bochum, Universitätsstr. 150, 44801 Bochum, Germany*
[3]*Institute for Physics and Astronomy, Technische Universität Berlin, Hardenbergstr. 36, 10623 Berlin, Germany*
[4]*Universität Paderborn, Warburger Str. 100, 33098 Paderborn, Germany*
[5]*Carl von Ossietzky Universität Oldenburg, Fakultät V, Institut für Physik, 26129 Oldenburg, Germany*
[6]*Institute of Theoretical Physics, Wrocław University of Science and Technology, Wrocław 50-370, Poland*
[7]*TUM School of Computation, Information and Technology, Technische Universität München, Hans-Piloty-Str. 1, 85748 Garching, Germany*

(Received 9 March 2026; accepted 10 August 2026; published 14 September 2026)

Tunnel-coupled optically active quantum dot molecules (QDMs) have the potential to operate as spin-photon interfaces with coupled spins that interact with two different photon frequencies at the same time. A prerequisite is to deterministically prepare two (electron or hole) spins in the QDM and be able to electrically tune the orbital state couplings. Here, we demonstrate the sequential optical charging of a single QDM with two-electron spins while simultaneously maintaining the ability to widely tune orbital couplings using static electric fields and optically drive the system for quantum light generation. We optically prepare one- and two-spin states, initialize via optical pumping and explore orbital and spin relaxation dynamics for one- and two-spin states as a function of the energy detuning and hybridization of orbital states. For two-spin states, remarkably long singlet-triplet relaxation times are observed, extending beyond ∼100 μs with strong dependence on the relative energy of ground and excited two-spin states. Qualitative agreement is observed with $\boldsymbol{k}\cdot\boldsymbol{p}$ calculations of phonon-mediated spin relaxation. Our results provide new quantitative understanding of the dynamics of one- and two-spin states and address a number of key prerequisites for using QDMs to create multidimensional photonic cluster states.

DOI: 10.1103/qgr2-968q

I. INTRODUCTION

Spin-photon interfaces can exploit light-matter interactions to generate non-classical states of light and mediate entanglement between non-interacting photonic qubits encoded in polarization, time or path degrees of freedom. In this context, optically active semiconductor quantum dots represent the gold standard for non-classical light sources. They are excellent on-demand single-photon emitters [1–3], can produce high-fidelity entangled photon pairs [4] and serve as reliable spin-photon interfaces [5–7]. Recently, single dots have been used to deterministically generate extended one-dimensional (1D) linear chains of entangled photons, so-called photonic cluster states [8–11]. However, multi-photon states with 2D entanglement structures are required for measurement-based quantum information processing [12]. Such states can be generated from 1D cluster states using probabilistic fusion gates [13], a process that does not scale as well with cluster state size. An alternative approach for deterministically generating cluster states with 2D entanglement structures is to use a pair of vertically stacked and coupled quantum dots, a quantum dot molecule (QDM) containing two interacting spins [14,15]. In these structures, the dots are separated by a thin tunnel barrier that couples the orbital states of trapped electrons or holes [16,17]. When populated by two spins, the hybridized orbital states promise longer spin coherence times due to the formation of noise-protected singlet-triplet (S-T) qubits in the two-spin

*Contact author: christopher.thalacker@tum.de

subspace [18–21]. This facilitates fast entangling operations on the two spins that can then be mapped into the photonic domain by optical driving at well-defined times [22–24]. Using a QDM for such applications requires the ability to deterministically host and initialize two-electron spins (i), a mechanism to tune the two electrons into a regime where their orbitals are hybridized over both dots (ii) and to perform single spin and entangling operations on the two spins in the molecule (iii). Moreover, the two-spin systems must have sufficiently long storage, relaxation and coherence times (iv), and finally, it must be possible to generate spin-photon entanglement with high photon indistinguishability over timescales faster than the tunneling-mediated singlet-triplet mixing (v). Requirements (i) and (ii) can each be individually fulfilled by embedding the QDM into the intrinsic region of a p-i-n diode and charging it using Coulomb blockade from a tunnel-coupled reservoir. However since a single control parameter—the axial electric field—is used to tune both orbital coupling and charge status, it has proven difficult to realize two-spin systems in widely tunable, optically active QDMs.

An alternative approach involves using charge storage devices [25] in which spins are *optically* prepared by resonant optical driving [25,26]. There, we demonstrate selective optical charging of a single QDM with one- or two-*electron spins*. After preparation, we show that one or two spins can be readily tuned into a regime where the orbital wave functions in the two dots hybridize, forming states with mixed spin and orbital character. This directly decouples requirements (i) and (ii). Moreover, we show that spin states in the QDM can be optically pumped over nanosecond timescales, and we measure the orbital and spin relaxation processes as the orbital coupling is electrically varied. Our results show that hybridized states can be repeatedly optically addressed before any charge loss occurs, with charges remaining in the QDM over timescales $\gg 50$ μs at 1.7 K. For the two-spin system, we show that it can be initialized into a well-defined singlet ground state that maintains its character even after electrical switching. We use our charge storage device to elucidate the relaxation dynamics of single- and two-electron spin states under optical pumping. The S-T relaxation is shown to be very slow for energy splittings $\Delta_{S-T} < 5$ meV, with relaxation rates as low as 0.01 μs^{-1}. Remarkably, upon increasing Δ_{S-T} beyond 5 meV, the relaxation rate suddenly increases by more than two orders of magnitude due to the onset of sequential multi-phonon spin relaxation via excited-state triplets.

In the context of cluster state generation we thus demonstrate the independent control of requirements (i) and (ii), including initialization of the two-spin system and furthermore long spin storage and relaxation times (iv). Point (iii) has been shown in past publications [23,24], as well as (v) for single dots [10,27] and to some extent quantum dot molecules [21]. The main challenge for genuine 2D cluster state generation is the reduction of the timescales for tunneling-mediated exchange coupling needed to generate entanglement to timescales slower than those for single-spin gates and photon generation.

II. DEVICE STRUCTURE, OPTICAL CHARGING AND SINGLE QDM EMISSION

As shown in Appendix A, our device consists of a single self-assembled QDM formed by a pair of vertically stacked InGaAs dots with a ∼10 nm dot-to-dot separation. The QDM is embedded into the intrinsic region of a p-i-n diode to apply static electric fields along the growth axis. The layer structure is designed for electron storage: the lower dot is flatter (larger confinement energy) than the upper quantum dot, and a 50-nm-thick AlGaAs barrier below the lower dot prevents the electrons from escaping (see also Appendix A). A circular Bragg grating (CBG) is deterministically fabricated directly above the QDM using *in situ* electron-beam lithography [28]. In this process, low-temperature cathodoluminescence is first employed to locate the molecule, after which electron-beam lithography defines and precisely aligns the CBG to the selected QDM [29]. In combination with a backside distributed Bragg reflector (DBR), this approach increases the efficiency of photon collection over a ∼10 nm bandwidth sufficient to simultaneously optically address transitions in the upper and lower dots [29]. Initially, we spectroscopically probe the orbital states of neutral and charged excitons in the QDM by performing voltage-dependent photoluminescence (PL-V) with a continuous wave (cw) laser at 850 nm, exciting quasi-free charge carriers in the wetting layer. For these PL-V measurements we prevent the accumulation of electrons in the QDM over time by applying a negative gate voltage V_G periodically to remove accumulated photogenerated electrons. This discharging phase is followed by a readout phase in which the QDM is excited. Figure 1(a) shows a typical example of such PL-V measurements. The data show strongly and weakly shifting lines indicating the presence of different indirect and direct excitonic complexes, along with avoided crossings as reported previously for QDMs [16,24,30]. Different charged complexes in the QDM can be readily identified by fitting the voltage-dependent emission energy of the different lines using a few-body Hamiltonian (see Appendix B). The model provides a consistent fit to the data, revealing neutral exciton states X^0 (red) with their characteristic anticrossing at $V_G = 0.56$ V, singly charged excitons X^- (blue) and doubly charged excitons X^{2-} (green) in the QDM. In Fig. 1(a) only the most relevant emission lines of X^- and X^{2-} are shown for clarity. The full set of transitions is shown in Appendix B. We further characterize the transitions via the orbital configuration of electrons and the holes, adopting the state labeling convention used in Ref. [17]. Here, the orbital configuration is

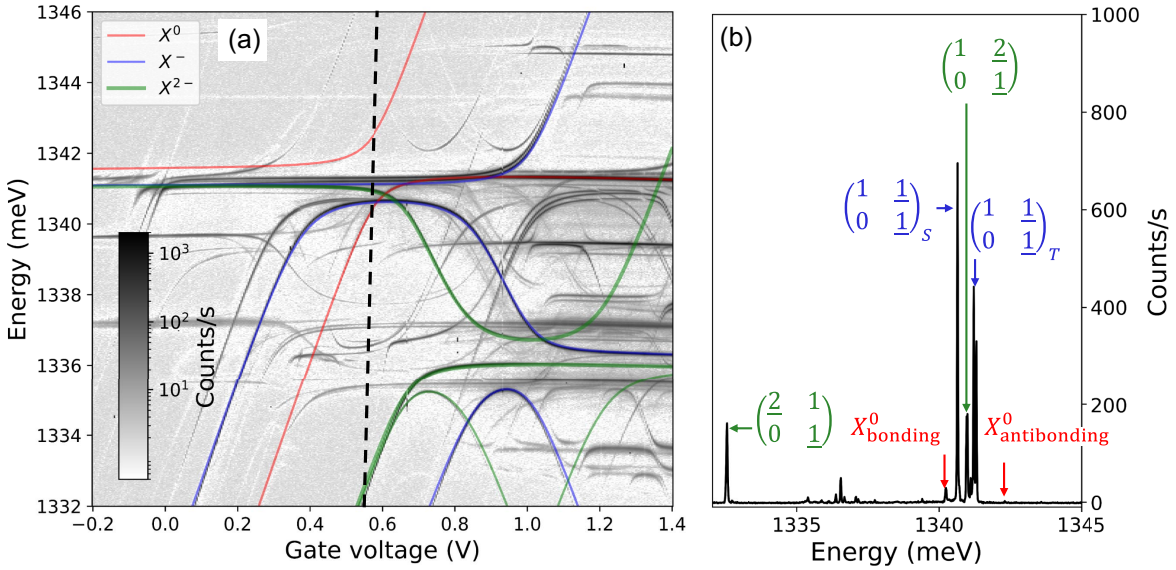

FIG. 1. Voltage-dependent photoluminescence (PL-V). (a) Voltage-dependent photoluminescence spectrum of a single quantum dot molecule. The most relevant transitions of different charged excitonic complexes are identified and overlaid with the spectrum in different colors. (b) PL-spectrum of the QDM at $V_G = 0.56$ V [marked by the dashed line in (a)]. Main transitions are labeled according to the convention explained in the main text.

denoted by a 2×2 matrix of the form:

$$\begin{pmatrix} e_l & e_u \\ h_l & h_u \end{pmatrix}, \tag{1}$$

where e_l (e_u) is the number of electrons in the lower (upper) dots and h_l (h_u) is the number of holes in the lower (upper) dots, respectively. When describing transitions, the underscores indicate which electron and hole recombine to generate the resulting photon. Figure 1(b) shows a selected spectrum recorded from the QDM at a gate voltage of $V_G = 0.56$ V and some of the most important transitions are labeled with the notation explained above. At this gate voltage, the electron state of the neutral exciton forms bonding and antibonding states that cannot be represented with the above notation, which is why they are explicitly labeled using subscripts.

For states not involving a hole (i.e. the bare one- and two-electron states), we also use a shorthand notation in the form of a row vector (e_l, e_u) where only the number of electrons in each dot is represented. Where necessary, the spin state of the two-electron system is denoted as a suffix to the orbital configuration of the form $(e_l, e_u)_s$ where $s \in \{S, T_0, T_+, T_-\}$, representing the symmetry of the two-spin states. In the results presented below, we discriminate between different voltage regimes. At low voltages, $V_G < 0.7$ V, the two-electron configuration $(e_L, e_U) = (2, 0)$ is energetically split off from the (1,1)-configuration by several millielectronvolts. We denote this to be the (2,0)-regime. Between $V_G = 0.8$ V and 1.2 V the lowest two-electron states are (1, 1)-states hybridized over both dots, forming singlet and triplet spin states (a more detailed description will be given in Sec. IV). We label this as the (1, 1)-regime where single-dot orbitals are hybridized. The regime where the (0, 2)-configuration forms the ground state ($V_G > 1.4$ V) is inaccessible in our device, since current begins to flow in the diode.

III. DETERMINISTIC TWO-ELECTRON CHARGING

The conventional method used to control the charge status of optically active quantum dots is to exploit Coulomb blockade between charges populating the dot and proximal Fermi reservoir [31]. Such stable two-spin regimes are typically achieved over a small region of the gate voltage space, defined by the orbital quantization energies (relative sizes) of the upper and lower dots, their relative In-Ga composition, and the distance of the QDM to the contact. This complicates free control of the detuning between the orbital states, without precise and independent control over geometry and composition. Here, we adopt an alternative approach that facilitates free tuning of the orbital energy separation in the two dots, whilst retaining two-electron spins within the system.

Hereby, we utilize an all-optical charging protocol that we previously demonstrated for single dots [32] and holes [25] in QDMs. In this charge control scheme, the controlled number of electrons in the molecule is defined by the four-stage protocol presented in Fig. 2(b). In step I (Reset), a large electric field (>140 kV/cm^{-1}) is applied that removes all residual charges by tunneling. Subsequently, in step II, the electric field is set such that the hole tunnels out faster than the exciton radiative lifetime,

and a resonant laser excites a neutral exciton in the lower dot of the molecule. This way, the QDM is deterministically charged by a single electron with near-unity efficiency. In step III, the same process can be repeated with the resonant laser tuned to the singly charged exciton X^-. Alternatively, the resonant charging laser can be fixed, and the electric field tuned to induce dc Stark shifts to sequentially tune the QDM into resonance with X^-. Finally, in step IV (Readout), the electric field is reduced, and the induced charge and spin states can be probed using resonance fluorescence as a function of the orbital coupling defined by V_G. Following the method presented in Ref. [25], we first determined the optimal parameters for sequential optical charging by mapping out the parameter space of charging voltage and charge laser energy. Full details are presented in Appendix D. Figure 2(a) shows different pairs of charging energy and voltage for one-electron charging (orange) and two-electron charging (purple). By tracing the voltage dependence and comparing it with the photoluminescence observed from charge states, where the hole is located in the lower dot [shown in Fig. 2(a)], the excitonic states via which charging occurs can be identified as $\left(\begin{smallmatrix}1 & 0\\ 1 & 0\end{smallmatrix}\right)$ for one-electron spin charging and $\left(\begin{smallmatrix}2 & 0\\ 1 & 0\end{smallmatrix}\right)$ for generation of the second spin. These assignments are confirmed by fitting the Hamiltonian to trace out the field-dependent excitonic states (see Appendix B). As shown in Fig. 2(a), very good agreement is observed with calculations of the voltage-dependent eigenenergies for the lower dot of the neutral exciton and singly charged exciton.

To demonstrate that this protocol deterministically prepares the desired number of electron spins in the QDM, we performed a control experiment depicted in Fig. 2(b). The charging laser is pulsed (200 ns duration, square pulse) and swept across the two charging voltage plateaus. The time offset between the onset of the charging laser and the beginning of the first charge voltage plateau is defined as Δt. In the readout stage ($V_G = 0.56$ V), we probe the resulting charge state by setting the readout laser to be resonant with the X^0, X^- or X^{2-} transition, respectively. Typical results are presented in Fig. 2(c). When the charge laser overlaps with the first charge voltage plateau, the X^0 transition measured in the readout phase of the experiment quenches, to be replaced by X^- at $\Delta t = -0.2$ μs. This observation confirms that a single electron is prepared in the QDM during the charging phases (II and III) of the protocol. As soon as the charge laser pulse temporally overlaps with both charge plateaus (II and III) at $\Delta t = 0$, the X^- signal quenches, and only emission stemming from X^{2-} is observed in the readout phase. As expected, when the charge laser pulse does not overlap with either plateau, the X^{2-} signal again vanishes, and only X^0 signal is observed. As for the previously studied hole storage sample in Ref. [25], we determined the charging fidelities to be above 85% which were obtained from

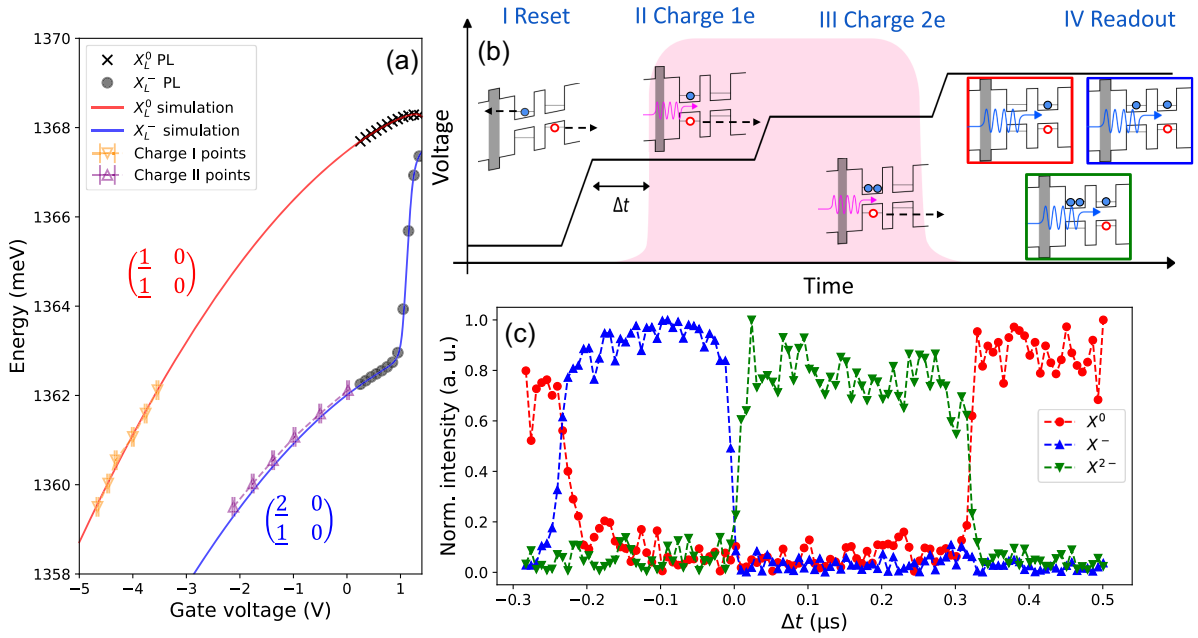

FIG. 2. Deterministic optical electron charging. (a) Voltage and energy points where 1e and 2e charging is possible. In the PL regime ($V_G > 0$ V) points where luminescence from the lower dot is directly observed are plotted for the X^0 and the X^-, along with a few-particle Hamiltonian simulation for these charged complexes. In the regime below 0 V, points where 1e and 2e charging occur (experimental data) are also marked. (b) Schematic of the sequential charging experiment. The charging laser pulse (indicated in magenta) is temporally scanned over the different voltage steps by an offset Δt that is measured relative to the start of the first charging plateau. The steps of the charging protocol are discussed in the main text. (c) Resonance fluorescence (RF) signal of X^0, X^- and X^{2-} vs the time offset of the charge laser pulse relative to the first charge voltage plateau.

comparing the observed photon counts in each charge state during different stages of the sequential charging experiment presented in Fig. 2(c). A detailed calculation of the charging fidelities can be found in Appendix E. We note that the main error source lies in the limited suppression of the resonant laser used to probe the charge states, which leads to significant background noise. The actual charging fidelity is likely much larger. We further note that a limited charging fidelity would not diminish the fidelity of a potential cluster state generated from the two electrons but would only have an influence on the generation rate. We furthermore report no observable reduction of the performance of our single QDM charge storage device over a time span of multiple months. Since the charging protocol relies only on the generic QDM level structure, we expect it to transfer to other QDM devices.

IV. SINGLET-TRIPLET REGIME

In the previous measurements, readout was performed at a gate voltage $V_G = 0.56$ V, where the two-electron ground state is (2,0) (two electrons in the lower dot, zero electrons in the upper dot). It is interesting to probe the situation when the orbital wave functions of the two electrons are hybridized over the two dots; the (1,1)-configuration and the Heisenberg coupling of the two spins is voltage tunable. Here, the electrons form hybridized singlet and triplet states that we denote as $(1,1)_S$ and $(1,1)_T$, separated by the singlet-triplet splitting Δ_{S-T}, determined by the orbital tunnel coupling between the dots [17]. This regime is also known as the "sweet spot," since the hybridized two-electron states are protected to the first order against electrical noise [19,33]. We energetically lift the degeneracy of the degenerate triplets T_+ and T_- by applying a magnetic field in the growth direction (Faraday geometry). The S_0 and T_0 states then form an optically isolated qubit that can be addressed via the (spin-polarized) doubly charged exciton states $R_+ = (\downarrow, \uparrow\downarrow\Uparrow)$ and $R_- = (\uparrow, \uparrow\downarrow\Downarrow)$ [17]. Figure 3(d) illustrates the energy level configuration of this system. From the PL-V measurements we identify this regime at a gate voltage $V_G = 1$ V (see also Appendix B).

To demonstrate that the singlet-triplet states can be optically addressed, we first show that the two electrons remain in the QDM over timescales much longer than needed for typical optical experiments. This is a key observation since it demonstrates that optical driving does not result in charge loss due to Auger processes or photo-ionization [34,35]. We do this by performing the

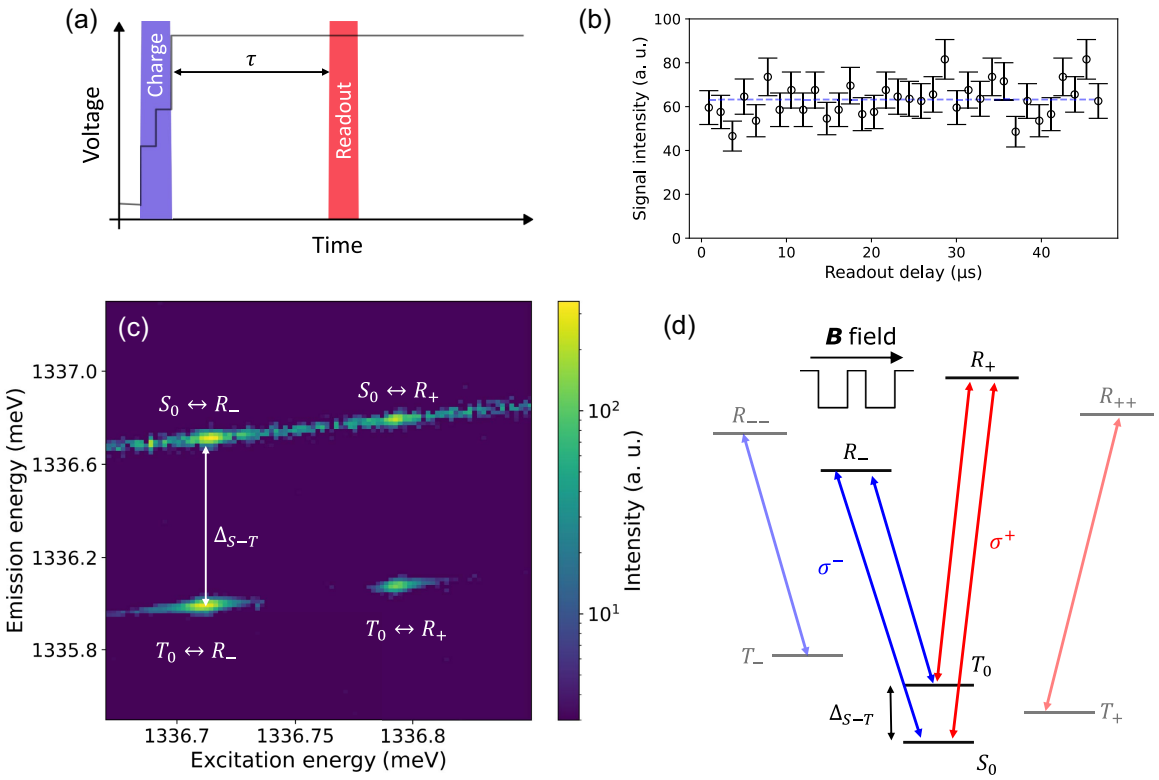

FIG. 3. Measurements on hybridized two-electron state. (a) Experimental method applied to measure the charge storage time. After the QDM is charged with two electrons, a short readout pulse resonant with the $S_0 \leftrightarrow X^{2-}$ transition probes the two-electron state throughout the readout phase IV of the experiment. (b) Intensity of the X^{2-} signal as a function of delay of the readout pulse relative to the charging phase. (c) RF scan over the hybridized two-electron state under application of an external magnetic field of 1 T (Faraday geometry). (d) Level scheme of the two-electron states and the doubly charged exciton states used for optical excitation.

experimental sequence depicted schematically in Fig. 3(a), where after charging the QDM with two electrons and moving them to the sweet spot, a short readout pulse delayed by a time τ probes the two-electron population. Due to electrons tunneling out of the QDM we expect an exponential decay of the X^{2-} signal with increasing delay time. Typical results obtained from such an experiment are presented in Fig. 3(b). Within experimental precision, we observe no decay of the X^{2-} signal for times between the preparation of the $2e^-$ spin state and probing it up to 50 µs. Hence, we conclude that the charge storage time is $\tau_{\text{storage}} \gg 50$ µs. We continue to investigate the optical excitation of the singlet-triplet qubit. Here, two electrons were again prepared before they were tuned to the sweet spot. A magnetic field of 1 T is used to lift the degeneracy of the spin-polarized triplet states. The energy of the readout laser pulse is then scanned over the singlet-trion transitions. The results of this scan are shown in Fig. 3(c). We observe two resonant transitions, $S_0 \leftrightarrow R_-$ and $S_0 \leftrightarrow R_+$ at 1336.713(23) and 1336.792(23) meV, respectively, as well as two non-resonant signals, which are the decays of the trion to the respective triplet states. These off-resonant transitions have an energy of 1335.995(23) meV ($T_0 \leftrightarrow R_-$) and 1336.076(23) meV ($T_0 \leftrightarrow R_+$). Away from the resonances, a background from the excitation laser is also visible, since the circular Bragg grating structure on top of the QDM limits the rejection of the scattered resonant drive laser by cross-polarized suppression between the excitation and detection channels. From the energy separation between the resonant and the non-resonant signal we directly read the singlet-triplet splitting Δ_{S-T}. For this sample it amounts to 718(16) µeV.

V. SINGLET INITIALIZATION

Preparation of the two-electron state via the lower dot trion initializes the electrons in a $(2,0)_S$-configuration. However, electrical switching to a different orbital configuration could potentially mix different orbital and spin states. In this section, we investigate this potential effect by performing the experiment shown in Fig. 4(a). Following the preparation of two electrons, the gate voltage is switched such that the electrons are in the (1, 1)-configuration. A 400 ns cw-laser pulse (red)

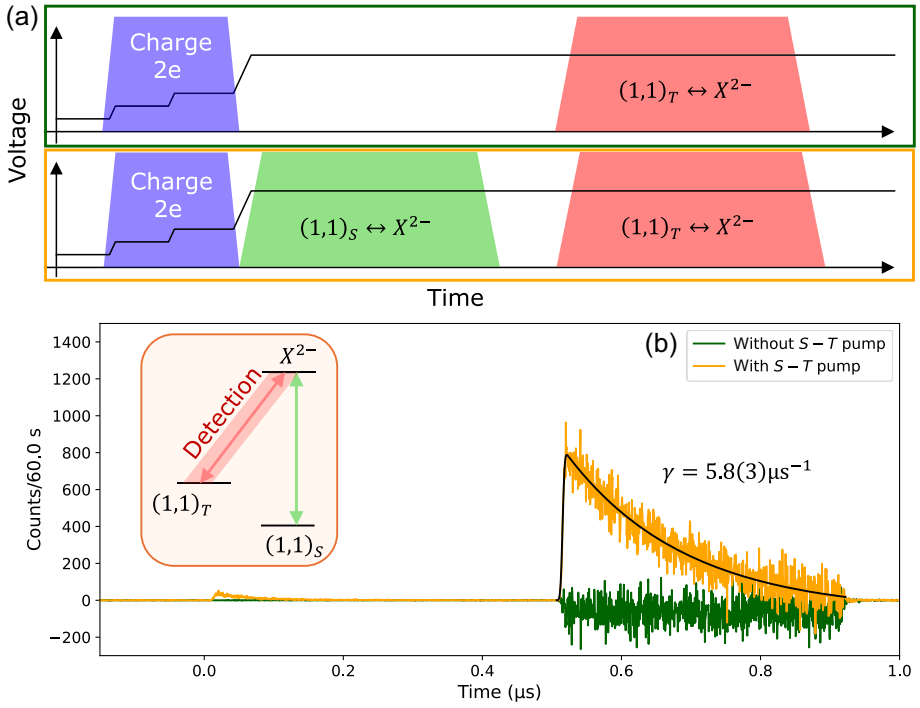

FIG. 4. Singlet initialization and probing of singlet-to-triplet transition in an optically controlled QDM. (a) Measurement scheme for demonstrating singlet initialization via charging. Following the preparation of two electrons, a probe pulse (red) resonant with the triplet-to-trion transition probes the spin population in the triplet state without (top) and with (bottom) a pump pulse (green) resonant with the singlet-to-trion transition prior to the triplet readout. (b) Time-resolved signal of the trion-to-triplet transition. Between 0.5 and 0.9 µs, a pulse resonantly probing the triplet population is applied. The signal was recorded without (green) and with (orange) a singlet-to-trion pump pulse applied prior to readout. A strong resonant trion-to-triplet signal is only observed when pumping the two-electron population from the singlet to the triplet first, indicating that the bare two-electron state after charging is mostly in the $(1,1)_S$ configuration. Inset: Level scheme of the two-electron state and the respective direct trion used for optical excitation. The ground state is the $(1,1)_S$ state. Optically driving the $(1,1)_S \leftrightarrow X^{2-}$ transition pumps the initial singlet population into the $(1,1)_T$ state.

resonantly probes the triplet population, and the recorded signal is analyzed in a time-resolved manner. The level scheme along with the excitation lasers and the detection filter setting is shown in the inset of Fig. 4(b) (see Appendix C for experimental details). The experiment is repeated in a second protocol, in which prior to probing the triplet population, another 400 ns cw-pulse [green arrow in the inset in Fig. 4(b)] drives the singlet-to-trion transition. This optically pumps the two-electron population from the $(1,1)_S$ state to the $(1,1)_T$ state. Figure 4(b) shows the time-resolved counts of the measurement sequence with and without the $S-T$ pump pulse. Without the $S-T$ pump pulse prior to probing the triplet population, no resonant triplet signal is observed (dark green time trace). In order to observe a resonant triplet signal, one needs to first shelve the population from the $(1,1)_S$ into $(1,1)_T$. This is done by using another cw-laser whose energy is resonant with the $(1,1)_S \leftrightarrow X^{2-}$ transition [light green pulse in the measurement sequence in Fig. 4(a)]. If this pump pulse is employed, then the triplet laser probes a significant resonant signal, which is shown by the orange time trace in Fig. 4(b). Besides the strong resonant signal of the probe pulse, a weaker signal of trion-to-triplet decay is also visible during the pump phase. This is a clear sign that the shelving of the two-electron state from the singlet to the triplet via the $X^{2-} \rightarrow (1,1)_T$ happens during pumping. Another observation is that the triplet signal is not constant in time but rather shows a decaying behavior. At the chosen probe power of 2 nW the decay rate was $5.8(3)\ \mu s^{-1}$. This observation is an indication of spin pumping occurring: the resonant triplet laser optically pumps the signal back to the singlet state. In the next section we continue to explore spin pumping and the relaxation between singlet and triplet states further.

We determine a lower bound for the spin initialization fidelity F_{init} from the charging process by comparing the signal observed during the triplet measurement, both with and without $S-T$ pump phase of the measurement protocol. The resonant triplet signal without the prior pump pulse directly measures the initial triplet population, which is vanishingly small. The limiting factor in this estimation stems from the subtraction of the residual resonant laser, which leads to substantial background noise. The triplet signal is buried by this noise, such that we estimate the maximum counts hidden within the laser background by measuring the 95% confidence interval $\sigma_{95\%}$. Multiplying this value by the on-time of the probe laser (400 ns) allows us to calculate the total number of photon counts $I_{\text{no pump},95\%}$ that could stem from residual triplet population without prior $S-T$ pump pulse. This value can be directly related to the total integrated counts I_{pump} of the triplet signal with the prior $S-T$ pump pulse active. We estimate the absolute lower bound for the fidelity $F_{\text{init}} = 1 - \frac{I_{\text{no pump},95\%}}{I_{\text{pump}}} \gg 61.2\%$. As mentioned, this low value is significantly underestimated since it is based on the unlikely assumption that a constant triplet signal may be buried within the laser background. Most likely, the actual initialization fidelity is much larger.

The measurements suggest that electrical switching does not change the singlet character of the initially prepared $(2,0)_{S_0}$-state. This is an expected result, since triplet and singlet electron states (in the absence of holes) are only weakly coupled by nuclear or external magnetic fields [36]. Mixing with higher energy singlet states remains a possibility; however even at the singlet anticrossing point, the energy gap between two singlet states is ~2 meV, or ~484 GHz. The adiabatic theorem [37,38] states that in order for singlet mixing to happen during electric switching, the switching speed needs to be in the same order of magnitude as the energy difference. The maximum bandwidth of the waveform generator is 100 MHz and therefore is over three orders of magnitude lower than the required speed to create singlet mixing.

VI. OPTICAL PUMPING OF ONE- AND TWO-ELECTRON STATES AND TRIPLET-SINGLET-RELAXATION

We continue by investigating optical pumping and relaxation of one- and two-electron states in the QDM. In the previous section it was already shown that under resonant excitation of the two-electron state, the state population can be optically pumped from a singlet to a triplet and vice versa, without a magnetic field. Our charge-tunable device facilitates measurement of the spin relaxation of the coupled electron system over a large range of orbital energy detunings to directly compare the situation to a single electron in the QDM. For two electrons, we uncover some intriguing and surprisingly slow dynamics.

We first compare optical pumping of the single-electron state and the two-electron state in a voltage regime, where the electron(s) orbital wave functions are mostly confined in the lower dot, i.e. the (1,0)-configuration and (2,0)-configuration, respectively. By optically exciting a singly (doubly) charged exciton in the upper dot, the system can either decay directly to its original state or indirectly with rate γ_{P} with the electron being effectively pumped into the upper dot. An electron in the upper dot will eventually relax back to the lower energy (1, 0)-state with rate γ_{rel}. The level schemes are depicted in Fig. 5 for (a) the single- and (b) the two-spin case. The recorded time traces of this resonant pumping are shown in Fig. 5(c). The blue trace in Fig. 5(c) shows the time trace of the single-electron case and compares it with the two-electron (green trace) upon resonant driving. A clear qualitative difference between the single-electron case and the two-electron case is visible: while the resonant signal remains constant when driving a single electron via the trion, driving the two-electron case via the doubly charged exciton reveals an exponential decay over nanosecond timescales. This is a

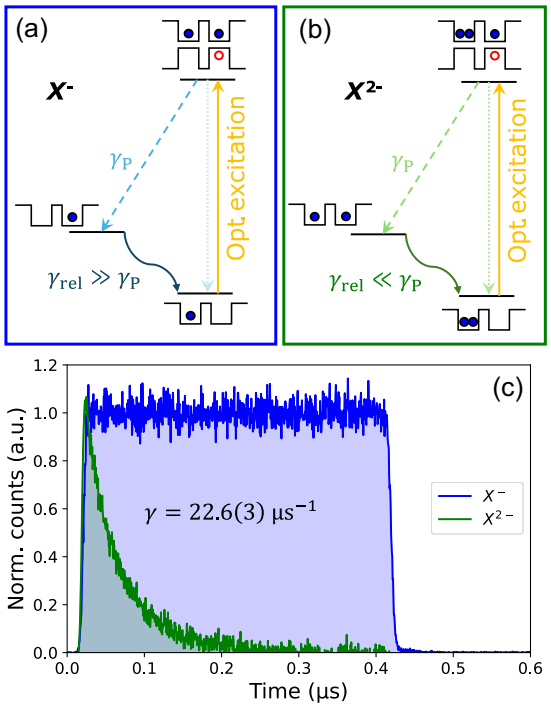

FIG. 5. Optical spin pumping level scheme for (a) one electron in the (1, 0)-configuration and for (b) two electrons in the (2, 0)-configuration. The yellow arrows indicate the optically driven transition, while the dashed blue (green) arrows show the possible recombination paths for the X^- (X^{2-}). (c) Optical driving of the one-electron (1, 0) and two-electron (2, 0) systems demonstrating Pauli blockade, and optical pumping of (2, 0) driven via the direct X^{2-}-transition.

clear indication of optical spin pumping. The absence of such a decay for a single electron can be understood by phonon-assisted tunneling: while the indirect transition does indeed occur and is also observed in luminescence, time-resolved studies have shown that inelastic interdot tunneling can occur over timescales ranging from ps → 100 ps [39]. This is much faster than the timescale of optical pumping, such that optical pumping is inhibited.

The fact that this is not observable in the two-electron case suggests that the relaxation from the (1, 1)-state back to the (2, 0)-state is inhibited by Pauli blocking and that the relaxation time is much longer than the timescale for optical pumping. In Appendix F, we present detailed calculations and analysis of the selection rules that lead to the spin pumping mechanism. The result is that for continuous pumping, the two-electron population becomes shelved from the $(2,0)_S$-state into the $(1,1)_{T_0}$, which is a metastable configuration with regard to the interdot-tunneling timescales. We quantify the stability of the $(1,1)_{T_0}$-state by directly measuring the relaxation time in a pump-probe-like experiment, where we first use a resonant cw-pulse to pump the $2e$ population from $(2,0)_S$ to $(1,1)_{T_0}$ and after some delay time we apply a second, identical pulse to probe how much of the population has relaxed back to (2, 0). This directly probes the triplet-singlet-relaxation rate. Figure 6(a) shows the probe histograms as a function of the delay time at $V_G = 0.56$ V. From the fit we can see that the relaxation takes place on a timescale of $\tau_{\mathrm{rel}} = 16.3(\pm 0.3)$ μs (corresponding to a relaxation rate of $\gamma_{\mathrm{rel}} = 0.061(2)$ μs^{-1}) and is thus significantly longer than the picosecond timescale expected for a single electron.

We measure the triplet-singlet relaxation rate over a larger voltage domain and thus different orbital configurations, from a regime where the (2, 0)-configuration is the ground state all the way to the hybridization regime at 1 V. The measured relaxation rates are shown in Fig. 6(b). At low voltages and thus large electric fields, the orbital character of the singlet ground state is mostly (2, 0) and the relaxation rate drops exponentially as a function of voltage. We thus model the voltage-dependent relaxation rate as a function:

$$\gamma_{\mathrm{rel}}(V) = \gamma_{\mathrm{rel},0} \exp(-\kappa(V - V_0)), \tag{2}$$

with some reference voltage V_0 and reference relaxation rate $\gamma_{\mathrm{rel},0} = \gamma_{\mathrm{rel}}(V_0)$. We find $\kappa = 187.57(10.71)$ V^{-1} until 0.54 V. After that, the exponential rate at which the relaxation rate decreases is lower, at $\kappa = 23.33(3.89)$ V^{-1} which continues until at least $V_G = 0.65$ V. The fact that the triplet-singlet-relaxation rate depends so strongly on the gate voltage signifies a strong electric field dependence, i.e. a strong dependence on the energy splitting of the orbital states involved. Furthermore, the two different timescales observed change rather abruptly in two different voltage domains, hinting toward different primary decay mechanisms being present in the two regimes. As a reminder, until a gate voltage of 0.75 V, the orbital character of the singlet ground state is predominantly (2, 0), while the triplet is always (1, 1). For $V_G > 0.65$ V the relaxation rate becomes too slow for us to experimentally probe it. However, toward the singlet hybridization regime for $V_G > 0.8$ V, we observe an increase in the relaxation rate, reaching $\gamma_{\mathrm{rel}} = 0.085(\pm 0.002)$ μs^{-1} in the sweet spot at $V_G = 1$ V. This increase is accompanied by the change of the orbital character of the singlet ground state from $(2,0)_S$ to $(1,1)_S$. This change is indicated in Fig. 6(b) by the background from white to blue. At the same time, the energy splitting between the $(1,1)_T$ state and the singlet ground state changes from being linearly dependent on the gate voltage to flattening out toward the sweet spot and reaching its minimum of 718 μeV. In Fig. 6(d) the blue curve shows the triplet-singlet energy splitting as a function of the gate voltage. The relaxation between two-electron states is much longer compared to the single-electron since relaxation from one of the triplet states inherently requires a spin-flip, as the spin projection of the two-electron system must change from

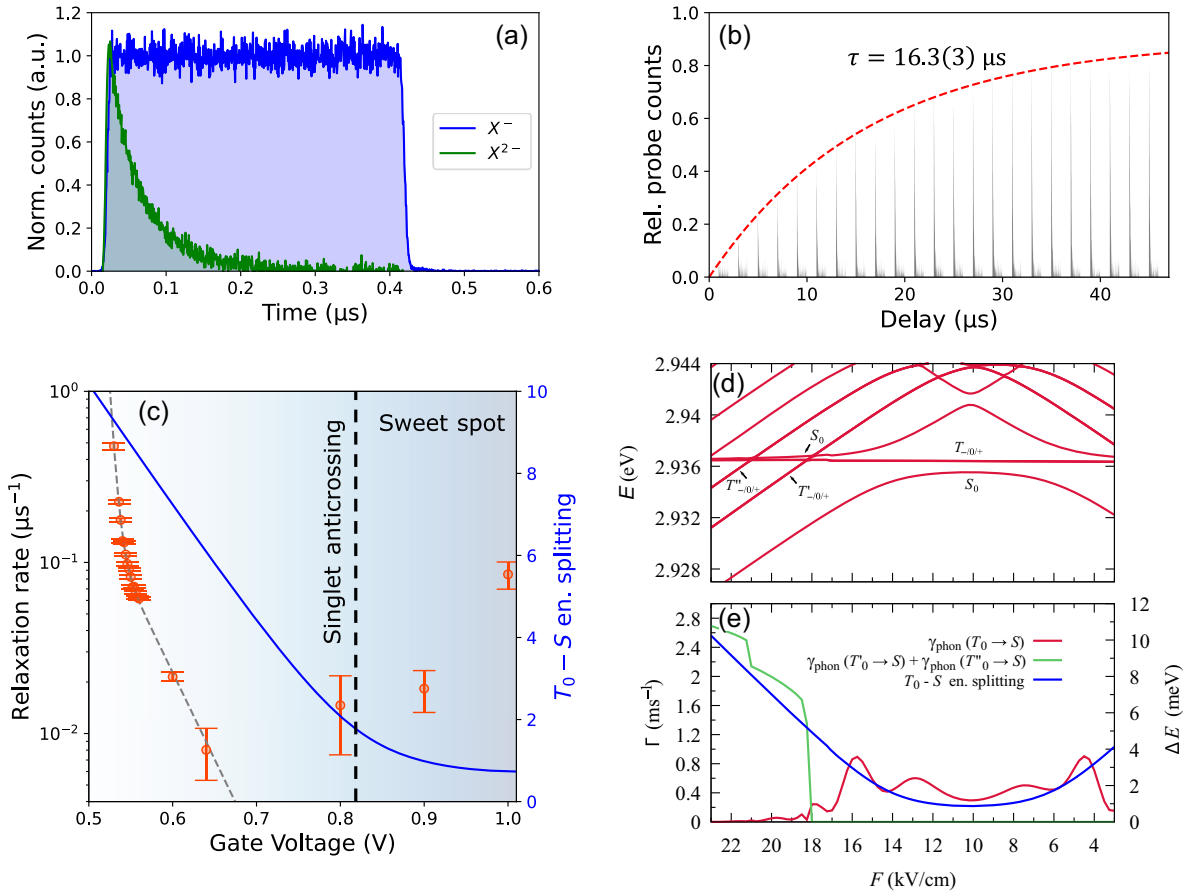

FIG. 6. Relaxation of two-electron states. (a) Typical results of pump-probe measurements consisting of optical driving of (2, 0) via the direct X^{2-} transition to the shelve population in (1, 1) before a delay without optical driving and a re-pump pulse to test relaxation from $(1,1) \to (2,0)$. (b) Orbital relaxation time measured from cw-pump-probe experiments as a function of the gate voltage. The anticrossing of (2, 0) and $(1,1)_S$ singlet states is marked by the vertical dashed line, and the $S-T$ sweet spot is close to 1.0 V. (c) Calculated field dependence of singlet and triplet states from the 8-band $k \cdot p$ modeling, revealing a sweet spot around 10 kV/cm. Note the higher energy triplet state shifting below the excited $(1,1)_{T_0}$ triplet at $F \geq 18$ kV/cm. (d) Calculated singlet-triplet-relaxation rates as a function of the electric field.

$M_S = 1$ to 0. Hence, spin-orbit-mediated spin relaxation must take place.

Recently, a theoretical analysis of triplet-singlet relaxation in QDMs was presented by some of us [40]. The approach is based on eight-band $k \cdot p$ theory and takes into account spin-orbit coupling that mixes pure spin states, thereby opening up channels for phonon-mediated relaxation [41,42]. Here, we employed this framework adapted to the size, shape and composition of the QDM studied. As discussed in more detail in Appendix G, the size, shape and In-composition profile of the QDM were adjusted to fit our optical spectroscopy data. The electric field dependence of the lowest-energy two-electron states was then computed by diagonalization of the Coulomb Hamiltonian using the configuration interaction method [43,44]. The calculated energies of the two-spin eigenstates are presented in Fig. 6(c) for the case with $B = 0.1$ T applied in Faraday geometry. This was chosen to be larger than the typical Overhauser fields for electrons in self-assembled dots, justifying neglecting hyperfine-mediated relaxation in our model [45]. We then computed the pure phonon-assisted spin-orbit-mediated relaxation rates between the two-electron energy levels, including electron-phonon interaction mediated by deformation potential and piezoelectric couplings [46–48] (see Appendix G). As shown in Fig. 17 in Appendix G, these rates are highly sensitive to the magnitude of the magnetic field. For illustrative purposes, we have chosen an arbitrary value of $B = 0.1$ T to demonstrate the qualitative behavior of the system. A direct comparison of the numerical values with experimental data (measured at $B = 0$) would, however, require including hyperfine-interaction-induced coupling, which lies beyond the scope of the present work. Furthermore, the agreement is affected by an uncertainty related to the exact double quantum dot morphology.

The two-spin eigenstates and the one- and two-step phonon-assisted relaxation rates, presented in Figs. 6(c) and 6(d), respectively, as a function of electric field.

Focusing first on the spin and orbital configurations at higher electric fields (e.g. $F \approx 22$ kV/cm), we note that the lowest-energy state is the spin singlet localized in the lower QD $|S_\ell\rangle$. The next two energetically higher-lying states, labeled $|T'_{-/0/+}\rangle$ and $|T''_{-/0/+}\rangle$, have triplet character and are each admixtures of s and p orbitals in the lower dot (see Appendix G). For orientation, the blue curve on Fig. 6(d) shows the field-dependent S-T splitting between $|T_{-/0/+}\rangle$ and $|S_0\rangle$. In the vicinity of the sweet spot ($F \approx 10$ kV/cm) we calculate an S-T splitting of 870 μeV, close to the experimentally measured value (718 μeV), confirming the general validity of our eight-band $k \cdot p$ model.

The field-dependent one-phonon (red curve) and sequential two-step phonon-assisted (green curve) relaxation rates are presented in Fig. 6(d). For $F > 10$ kV/cm, both $|T'_{-/0/+}\rangle$ and $|T''_{-/0/+}\rangle$ progressively shift energetically below $|T_{-/0/+}\rangle$. This is accompanied by a rapid increase in the two-step phonon relaxation rate (green curve), an observation qualitatively consistent with the rapid increase in the two-spin relaxation rate observed experimentally for gate voltages below 0.54 V [Fig. 6(b)]. Fundamentally, the rapid increase arises from transitions via intermediate triplet states involving p-shell orbitals in the lower dot.

The calculated total phonon-mediated relaxation rates are ∼50× smaller than we observe in the experiment. However, we note that our measurements were performed at zero magnetic field, where phonon-assisted hyperfine spin-flips may also contribute significantly to the relaxation. Until now phonon-assisted hyperfine spin-flips have only been theoretically studied in QDMs for single-electron-doped dots [49]. Moreover, relaxation rates are likely to be strongly impacted by the precise admixture of s- and p-orbitals in the triplet and lower singlet states. This depends on the precise orbital level structure of QDMs, likely to be a complex function of size, shape and in-composition. As such, quantitatively taking into account all different states and relaxation pathways, particularly in the two-particle case, is expected to be non-trivial. We consider the qualitative agreement between experiment and theory to be satisfactory, and the qualitatively similar electric field dependence provides good evidence that one- and two-step phonon-mediated processes are indeed responsible for relaxation. Further investigations are required to fully understand the role of hyperfine coupling in the QDMs.

VII. QUANTUM INFORMATION RELEVANCE

Our results demonstrate that a QDM with independent control of charge state status and orbital coupling achieves high charge storage times (>50 μs) and high spin lifetimes (>10 μs). These timescales are certainly larger than the typical spin coherence times in self-assembled quantum dots of a few nanoseconds, limited by coupling to the fluctuating nuclear spin environment, which is the primary limiting factor of spin-photon interfaces in such systems so far. Here, we provide an estimation of the potential for our system in the context of multidimensional photonic cluster state generation. The current state-of-the-art generation of a photonic cluster state in a self-assembled quantum dot was presented in Ref. [11], where a three-photon linear cluster state was demonstrated with three-partite fidelity of $F_3 = 63(5)\%$, photon indistinguishability $M = 88.0(5)\%$ and a heralded three-photon rate of 14 kHz. The fidelity in this publication was mostly limited by spin dephasing of the host electron spin due to interactions with the nuclear field. To extend the entanglement of such a source into the second dimension, two such states need to be fused using a type-II fusion operation [13]. The success rate of such a fusion operation is ideally given by $p_f = \frac{M}{2} = 0.44$ and to obtain a $2 \times n$ grid cluster state, at least n such fusion operations need to be performed. Therefore, the success probability for generating such a state assuming ideal fusion operations is limited to

$$p_n^{\text{fusion}} = \left(\frac{M}{2}\right)^n = (0.44)^n, \tag{3}$$

which is the final fidelity limit for "cross-linking" two linear cluster states from the source presented in Ref. [11].

On the other hand, by integrating the QDM into an electrically contacted photonic structure similar to that presented in Ref. [11] (a similar device was presented in Ref. [50]) we estimate that two chains of entangled photons can potentially be generated from the QDM with similar fidelity as in Ref. [11]. For a two-dimensional cluster state, the limiting factor would then not be photon indistinguishability, which leads to reduced fusion fidelity, but the fidelity at which entanglement can be generated between the two spins in the QDM. The protocol presented in Ref. [15] proposes entanglement generation-based single-spin rotations and free evolution of the coupled spin system. As such, the limiting factor in this scenario is the fidelity of the single spin rotations and the different g-factor in each dot forming the molecule for realistic dots that calls for eight such rotations. In Ref. [23] single-spin rotations in a QDM have been shown with a fidelity of $F_{1e} = 0.98$. Combined with our spin preparation fidelity of $F_{\text{init}} > 0.61$ we infer that in our structure the cross-linking fidelity for an $2 \times n$ cluster state would be

$$p_n^{\text{QDM}} = 0.61 \cdot F_{1e}^{8n} \approx 0.61 \cdot (0.85)^n, \tag{4}$$

which is already larger than the cross-linking fidelity obtained from fusion operations for $n = 1$. Moreover, we emphasize that the initialization fidelity could be

further increased by adding an additional optical spin preparation step. The limited charge preparation fidelity of 85% does not limit the attainable entanglement fidelity of the system, as already stated in Sec. III, since deficient charge preparation leads to failure of any subsequent protocol and would thus only limit the attainable generation rates.

VIII. CONCLUSION AND OUTLOOK

In summary, we demonstrated the sequential optical charging of a single QDM with two-electron spins while simultaneously maintaining the ability to widely tune orbital couplings using static electric fields and optically drive the system for quantum light generation. We optically prepared one- and two-spin states with charge preparation fidelities exceeding 85%, initialized via optical pumping, and explored orbital and spin relaxation dynamics for one and two-spin states as a function of the energy detuning and hybridization of orbital states and thus successfully decoupled spin preparation and initialization from the orbital coupling condition, a key step toward better control of two-electron spin states in quantum dot molecules. Our system furthermore allowed us to selectively probe and compare dynamics of single-spin and two-spin states. For two-spin states, remarkably long S-T relaxation times were observed, extending beyond $\sim$100 μs with strong dependence on the relative energy of ground and excited two-spin states. Semi-quantitative agreement was observed with $\boldsymbol{k}\cdot\boldsymbol{p}$ calculations of phonon-mediated spin relaxation.

Our work demonstrates that charge storage devices can be used to deterministically prepare two electrons in a quantum dot molecule with hybridized orbital states. In the future, such a device can be used to show coherent spin control of the two-spin system. In combination with deterministic spin-photon entanglement, which has been demonstrated for single quantum dots in the past, this paves the way for the generation of deterministic two-dimensional photonic cluster states. One necessary improvement to achieve two-spin control in such structures is the further reduction of the tunnel coupling strength, such that entanglement between the spin states is mediated on the timescales of spin-photon entanglement generation.

ACKNOWLEDGMENTS

J. J. F. and K. M. gratefully acknowledge funding by the Bavarian Hightech Agenda within the Munich Quantum Valley. We acknowledge the BMFTR for financial support via the QR.N consortium via sub-projects FKZ 16KIS2197 (J. J. F.), 16KIS2200, 16KIS2203, 16KIS2193 (S. R.), 16KIS2203 (C. G.), and 16KIS2206 (D. R.), the QUANTERA EQSOTIC project 16KIS2061. We gratefully ackowledge financial support via the EUROSTARS QTRAIN project 13N17328. We are very grateful to the Deutsche Forschungsgemeinschaft (DFG, German Research Foundation) for financial support under Germany's Excellence Strategy—EXC-2111, DIP (FI 947/6-1), the ML4QL Cluster of Excllence (EXC 2004/1) and the MCQST Cluster of Excellence (EXC-2111). We also gratefully acknowledge—390814868 and project CNLG (MU 4215/4-1) (K. M.). K. G. and J. J. F. acknowledge the DAAD-NAWA for financial support via the center-to-center exchange Grant No. 57754510. The project is co-financed by the Polish National Agency for Academic Exchange.

DATA AVAILABILITY

The data that support the findings of this article are not publicly available upon publication because it is not technically feasible and/or the cost of preparing, depositing, and hosting the data would be prohibitive within the terms of this research project. The data is available from the authors upon reasonable request.

APPENDIX A: SAMPLE DESIGN

The measurements were performed on two vertically stacked InAs quantum dots embedded in a GaAs matrix. The quantum dot heterostructure is schematically shown in Fig. 7(a). It was grown by molecular beam epitaxy in the Stranski-Krastanov growth mode, where the lower and upper dots were In-flushed to a height of 2.7 and 2.9 nm, respectively. The total separation between the two dot layers is 10 nm. The separating layer mostly consists of GaAs, but 2.5 nm of it is made from $Al_{0.34}Ga_{0.66}As$ to further reduce the tunnel coupling strength between the stacked dots. 5 nm below the lower quantum dot layer there is a 50 nm $Al_{0.34}Ga_{0.66}As$ layer that serves as a tunneling barrier for electrons trapped in the quantum dots. The whole structure is sandwiched by a *p*-doped layer (top) and an *n*-doped layer (bottom) for electrical contacting. To increase the photonic out-coupling efficiency, a DBR is located at the bottom of the layer structure, combined with a CBG that is deterministically etched on top of individual QDMs using *in situ* electron-beam lithography at 10 K [29]. These are then embedded into a p-i-n diode, where the QDMs are contacted individually by metallic front contact. An electric field is applied to the (individual) QDM by applying a gate voltage V_G between the two contacts. The *p*-layer of the diode is kept small (25×8 μm) to keep its capacitance low and therefore electrical switching times short. To make the contacts smooth, an insulating bridge, made from SU-8 resist, was fabricated first. A schematic cross section of the device is shown in Fig. 7(b), while Fig. 7(c) shows a microscope image of a real fabricated device.

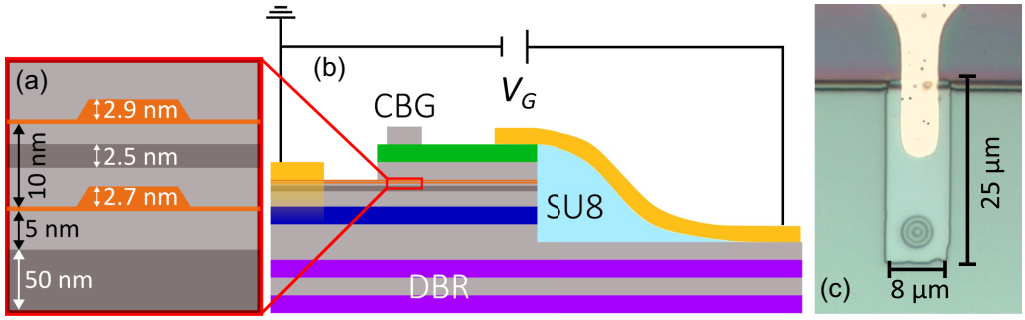

FIG. 7. Sample design (a) Schematic close-up to the two tunnel-coupled quantum dots with the relevant measures. Light-gray shaded areas represent the GaAs matrix, while dark-gray shaded areas represent $Al_{0.34}Ga_{0.66}As$-barriers. The orange-shaded area shows the stacked quantum dots with the wetting layers below them. (b) Schematic cross section of the full layer structure and device. The green layer is the *p*-doped layer, while the dark blue layer is the *n*-doped layer. The *n*-contact on the left does not directly touch the *n*-doped layer but is thermally annealed to it. DBR: Distributed Bragg reflector, CBG: Circular Bragg grating. (c) Microscope image of the fabricated device.

APPENDIX B: IDENTIFICATION OF DIFFERENT CHARGE STATES

In this section we discuss the identification of the different charged complexes observed in the voltage-dependent photoluminescence spectra presented in Sec. II of the main text. We use phenomenological few-spin Hamiltonians that take into account Coulomb interactions between the particles, as well as coherent tunnel coupling, which govern the voltage dependence of the observed PL lines. Effects that cannot be resolved by this PL method, e.g. the electron-hole-exchange interaction, are omitted here. The identification of the charged complexes from the PL-V assists us in finding the resonant energies used in the experiments in Secs. III–VI. The discussions closely follow the models presented in Ref. [17].

1. Neutral exciton

The voltage-dependent PL-V spectra show different charged excitonic complexes. From this data, we can identify the neutral exciton (X^0), the singly charged exciton (X^-) and the doubly charged exciton (X^{2-}) by modeling the different direct and indirect charge configurations [17,29]. Using the notation explained in the main text, we can write the neutral exciton with the basis states:

$$\begin{pmatrix} 1 & 0 \\ 0 & 1 \end{pmatrix}, \qquad \begin{pmatrix} 0 & 1 \\ 0 & 1 \end{pmatrix}. \tag{B1}$$

In this basis we can express the Hamiltonian of the X^0 as (omitting the electron-hole exchange interaction):

$$\hat{H}_{X^0} = E_{X^0} \cdot \hat{I} + \begin{pmatrix} \Gamma_{X^0} - f & t \\ t & 0 \end{pmatrix} + \begin{pmatrix} pF + \alpha F^2 & 0 \\ 0 & pF + \alpha F^2 \end{pmatrix}, \tag{B2}$$

where E_{X^0} is the emission energy of the direct exciton with no electric field applied, Γ_{X^0} is the energy mismatch between the electron levels in the upper and the lower dot, including Coulomb interaction between the electron and the hole, t is the tunnel coupling strength of the electron levels and $f = edF$ with e the elementary charge, d the distance between the two dots and F the applied electric field. The last term in (B2) contains the terms related to the quantum confined Stark effect. Here, p denotes the intrinsic dipole moment and α the polarizability. The electric field F can be obtained from the applied gate voltage V_G using:

$$F = \frac{V_{\mathrm{bi}} - V_G}{D}, \tag{B3}$$

where V_{bi} is the built-in voltage of the diode and D is the width of the diode's intrinsic region. For a p-i-n diode in GaAs the built-in voltage is $V_{\mathrm{bi}} = 1.51(1)$ V. The width of the intrinsic region $D = 365$ nm is known from the sample growth. Diagonalizing the Hamiltonian Eq. (B2) will give us the eigenenergies of X^0 as a function of the applied gate voltage V_G. Since the neutral exciton recombines to the crystal ground state, these eigenenergies correspond to the

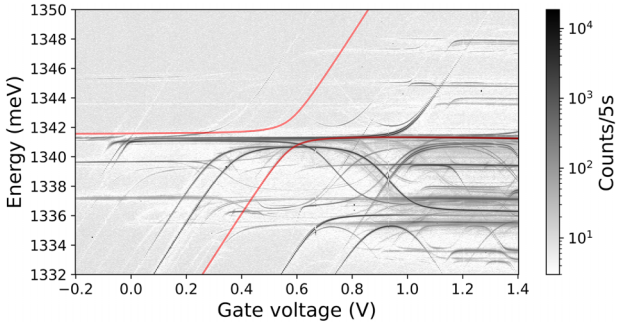

FIG. 8. Photoluminescence spectrum overlaid with the X^0 energies obtained from the model explained in the main text.

emission energies observed in the PL-V measurement. Therefore, the PL-V spectrum allows us to determine the parameters used in this model. Figure 8 shows the PL-V spectrum overlaid with the neutral exciton energy we obtain from our model. The determined parameters are listed in Table I.

TABLE I. Neutral exciton parameters determined from voltage-dependent photoluminescence.

Parameter	Value
E_{X^0}	1341.3(1) meV
d	10.9(1) nm
t	1.0(1) meV
Γ_{X^0}	27.8(1) meV
p	$0.14(5)e \cdot$ nm
α	$-18(6)e \cdot \mathrm{nm}^2/\mathrm{V}$

2. Single-charged exciton

In a similar fashion we obtain the emission energies for the singly charged exciton. It consists of two electrons and one hole, where the hole is again located in the upper dot. Since there are now two electrons in the QDM, spin effects need to be taken into account, as well. Expanding the notation introduced in the previous section, we can express the Hamiltonian in the following basis [51]:

$$\begin{pmatrix} \uparrow\downarrow & 0 \\ 0 & \Uparrow \end{pmatrix}, \quad \begin{pmatrix} \uparrow & \downarrow \\ 0 & \Uparrow \end{pmatrix}_S, \quad \begin{pmatrix} \uparrow & \downarrow \\ 0 & \Uparrow \end{pmatrix}_{T_0}, \quad \begin{pmatrix} \uparrow & \uparrow \\ 0 & \Uparrow \end{pmatrix}_{T_+}, \quad \begin{pmatrix} \downarrow & \downarrow \\ 0 & \Uparrow \end{pmatrix}_{T_-}, \quad \begin{pmatrix} 0 & \uparrow\downarrow \\ 0 & \Uparrow \end{pmatrix}. \tag{B4}$$

The suffices indicate whether the spins are configured as a singlet (S) or triplet (T). In this basis we can express the Hamiltonian of the tunnel-coupled system as:

$$\begin{aligned} \hat{H}_{X^-} &= E_{X^-} \cdot \hat{I} + (pF + \alpha F^2) \cdot \hat{I} \\ &+ \begin{pmatrix} \Gamma_{ll}^{X^-} - 2 \cdot f & \sqrt{2}t & 0 & 0 & 0 & 0 \\ \sqrt{2}t & \Gamma_{lu}^{X^-} - f & J_{eh} & 0 & 0 & \sqrt{2}t \\ 0 & J_{eh} & \Gamma_{lu}^{X^-} - f & 0 & 0 & 0 \\ 0 & 0 & 0 & \Gamma_{lu}^{X^-} - f + J_{eh} & 0 & 0 \\ 0 & 0 & 0 & 0 & \Gamma_{lu}^{X^-} - f - J_{eh} & 0 \\ 0 & \sqrt{2}t & 0 & 0 & 0 & 0 \end{pmatrix}, \end{aligned} \tag{B5}$$

where E_{X^-} is the energy of the direct trion in the upper dot $\left(\begin{smallmatrix} 0 & 2 \\ 0 & 1 \end{smallmatrix}\right)$, the $\Gamma_{ij}^{X^-}$, $i, j \in \{l, u\}$ are energy corrections when finding the electrons in the lower (l) or upper (u) that stem from the energy mismatch of the two dots, as well as different Coulomb energies. J_{eh} is the electron-hole exchange interaction, which is non-negligible for the coupled two-electron system with a localized hole.

The single-electron basis that we use is (omitting spin again)

$$\begin{pmatrix} 1 & 0 \\ 0 & 0 \end{pmatrix}, \quad \begin{pmatrix} 0 & 1 \\ 0 & 0 \end{pmatrix}. \tag{B6}$$

In this basis, the Hamiltonian reads

$$\hat{H}_{e^-} = \begin{pmatrix} \Gamma_{e^-} - f & t \\ t & 0 \end{pmatrix}, \tag{B7}$$

where Γ_{e^-} is the energy mismatch between the single confined electron levels of the upper and lower dots. We obtain the emission energies of the singly charged exciton by diagonalizing the trion Hamiltonian (B5) and the single-electron Hamiltonian (B7) and then subtracting the single-electron eigenenergies from the trion eigenenergies. Again, this method allows us to determine the parameters of the model by comparing the transition energies obtained from the model to the emission energies of the PL-V spectrum. The PL-V along with the modeled transition energies is shown in Fig. 9. The found parameters are listed in Table II. Parameters that are the same for

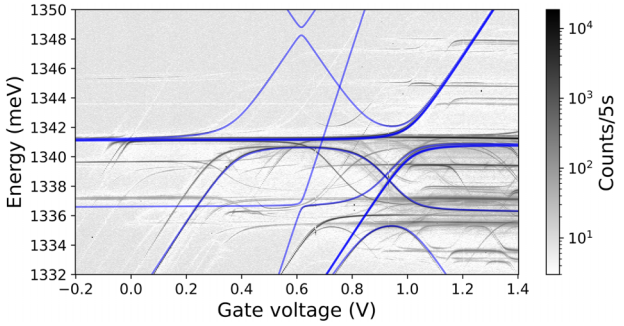

FIG. 9. Photoluminescence spectrum overlaid with the X^- energies obtained from the model explained in the main text.

TABLE II. Single-charged exciton parameters determined from voltage-dependent photoluminescence.

Parameter	Value
E_{X^-}	1336.3(1) meV
$\Gamma_{ll}^{X^-}$	52.9(1) meV
$\Gamma_{ul}^{X^-}$	19.4(1) meV
J_{eh}	0.1(1) meV
Γ_{e^-}	14.8(1) meV

each charged complex and were already listed in Table I are not repeated here.

3. Double-charged exciton

From the emission energy we can also identify the doubly charged exciton (three electrons, one hole in the upper dot). For this, we consider the doubly charged exciton in the basis:

$$\begin{pmatrix} 2 & 1 \\ 0 & 1 \end{pmatrix}, \qquad \begin{pmatrix} 1 & 2 \\ 0 & 1 \end{pmatrix}. \tag{B8}$$

We note once more that here the electron-hole-exchange interaction was omitted for simplicity. In Appendix F it will become relevant. The Hamiltonian in this basis reads

$$\hat{H}_{X^{2-}} = E_{X^{2-}} \cdot \hat{I} + (pF + \alpha F^2) \cdot \hat{I} + \begin{pmatrix} \Gamma_{X^{2-}} - f & t \\ t & 0 \end{pmatrix}, \tag{B9}$$

where $E_{X^{2-}}$ is the energy of the direct doubly charged exciton in the configuration $\left(\begin{smallmatrix} 1 & 2 \\ 0 & 1 \end{smallmatrix}\right)$ and $\Gamma_{X^{2-}}$ is the doubly charged exciton equivalent to Γ_{X^0}. We can further write the Hamiltonian of the two-electron system in the two-electron basis:

$$\hat{H}_{e^{2-}} = \begin{pmatrix} \Gamma_{ll}^{e^{2-}} - f & \sqrt{2}t & 0 & 0 & 0 & 0 \\ \sqrt{2}t & 0 & 0 & 0 & 0 & \sqrt{2}t \\ 0 & 0 & 0 & 0 & 0 & 0 \\ 0 & 0 & 0 & 0 & 0 & 0 \\ 0 & 0 & 0 & 0 & 0 & 0 \\ 0 & \sqrt{2}t & 0 & 0 & 0 & \Gamma_{uu}^{e^{2-}} + f \end{pmatrix}. \tag{B10}$$

Here, $\Gamma_{uu}^{e^{2-}}$ ($\Gamma_{ll}^{e^{2-}}$) is the energy bias that needs to be applied when both electrons are found in the upper (lower) dot. Note that here, unlike for Eq. (B5), we chose an energy reference where the (1,1)-configuration has a fixed energy of 0. Without an external magnetic field the three triplet states are degenerate. Again, we obtain voltage-dependent transition energies when diagonalizing the Hamiltonians Eqs. (B9) and (B10) and subtracting the resulting spectra. We can again use the model to identify the transitions in the PL-V spectrum and determine the QDM parameters for the X^{2-}. The PL-V overlaid with the transition energies obtained from fitting the PL-V with the model is shown in Fig. 10. Once the parameters are obtained, we can look at the voltage-dependent eigenenergies of the two-electron state that we get from diagonalizing the Hamiltonian Eq. (B10). These eigenenergies are shown in Fig. 10(b). The energy scale is chosen to be zero if the electrons occupy different QDs. One can see that around $V_G = 1$ V, the orbital wave functions of the electrons hybridize over the two QDs and form the well-known singlet-triplet ground states. This regime is also commonly referred to as sweet spot, and it is marked as a blue area in Figs. 10(a) and 10(b). The parameters for the doubly charged exciton, found from the PL-V, are listed in Table III.

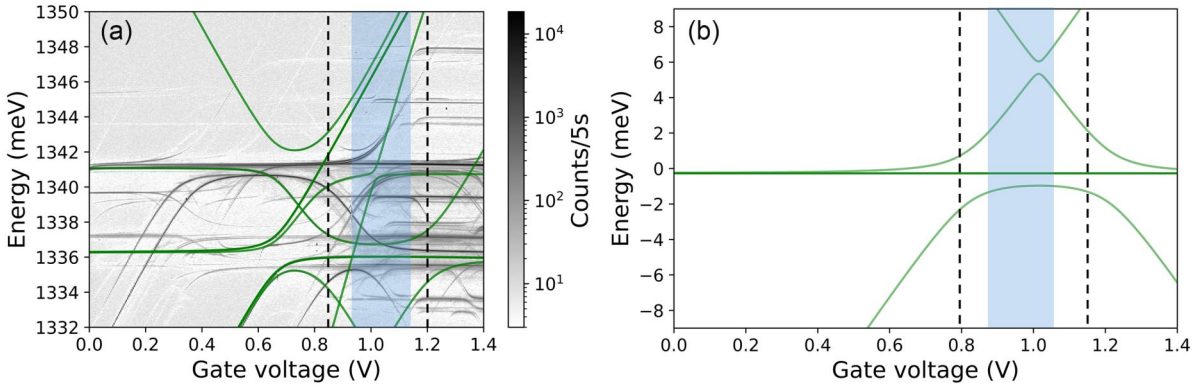

FIG. 10. (a) Voltage-dependent photoluminescence spectrum overlaid with the X^{2-} energies obtained from the model explained in the main text. (b) Voltage-dependent two-electron-eigenenergies determined from diagonalizing the Hamiltonian Eq. (B10) and using the parameters determined from fitting the transition energies with the model explained in the main text. In both figures, the sweet spot (hybridization regime of the two electrons) is shaded in light blue.

TABLE III. Double-charged exciton parameters determined from voltage-dependent photoluminescence.

Parameter	Value
$E_{X^{2-}}$	1336.0(1) meV
$\Gamma_{X^{2-}}$	25.2(1) meV
$\Gamma_{ll}^{e^{2-}}$	20.5(1) meV
$\Gamma_{uu}^{e^{2-}}$	−9.2(1) meV

APPENDIX C: EXPERIMENTAL SETUP

The experimental setup used for the charging experiments is illustrated schematically in Fig. 11. The lasers used for charging, readout and pumping are tunable diode lasers (two Toptica CTL and one Toptica DLPro) gated using acousto-optic modulators (AOMs) (AA Opto-electronic MT250-IR6). They receive their signal from an arbitrary waveform generator (AWG) (Tektronix AWG5204) that furthermore triggers the signal output of a second waveform generator (Keysight 33500B) to gate the sample diode, thus synchronizing the lasers and the gate voltage signal. We use a confocal microscope with a 0.81 NA objective lens to achieve laser excitation and fluorescence collection, where the excitation and detection paths are split by a non-polarizing 50:50 beam splitter. To filter out resonant laser light, we use cross-polarized detection of the emitted photons, where two linear polarizers (LPs), one in the excitation path and one in the detection path, are set such that their polarizations are orthogonal. An additional quarter wave plate is used to correct for small residual elliptical components in the excitation light. Not shown in the figure is a fourth laser emitting at 850 nm used to measure voltage-dependent photoluminescence via excitation of charge carriers in the wetting layer. It is possible to either measure spectral properties of the emitted photons using a double monochromator and liquid nitrogen-cooled CCD or to perform time-resolved measurements by counting (spectrally filtered) photons using a single photon avalanche diode (SPAD) (Excelitas SPCM-AQRH-16-FC) and time-correlating them with the waveform signals using a time-tagging unit (Swabian Instruments Time Tagger Ultra).

APPENDIX D: DETERMINING CHARGING PARAMETERS

For charging the QDM with one electron, we used a charge laser energy of 1361.0 meV. This will charge the QDM with one electron at a gate voltage of −4 V during the first charging phase. To charge the QDM with a second

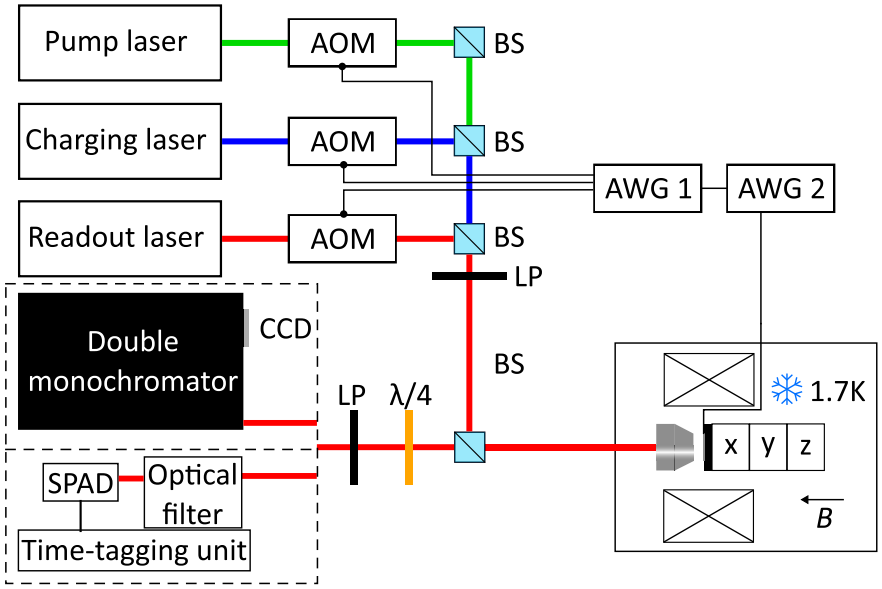

FIG. 11. Schematic of the experimental setup. Three continuous wave lasers are passed through AOMs. The AOMs are gated using an AWG 1. The lasers are combined using non-polarizing beam splitters (BS) and guided to the sample that is built into a cryostat (Attocube2100) and held at 1.7 K. The sample is placed on nanopositioners (Attocube ANP). A second AWG sets the voltage sequence that is applied to the QDM. Via a superconducting solenoid magnet, a magnetic field of up to 9 T can be applied in the growth direction of the sample (Faraday geometry). Luminescence photons of the dot are collected and either analyzed using a double monochromator and a liquid nitrogen-cooled CCD to obtain spectral data or after optical filtering, can be analyzed in the time domain using a SPAD and subsequent time-tagging unit. Polarization control and suppression of the excitation laser and the emitted photons is facilitated by using LPs and a quarter wave plate ($\lambda/4$).

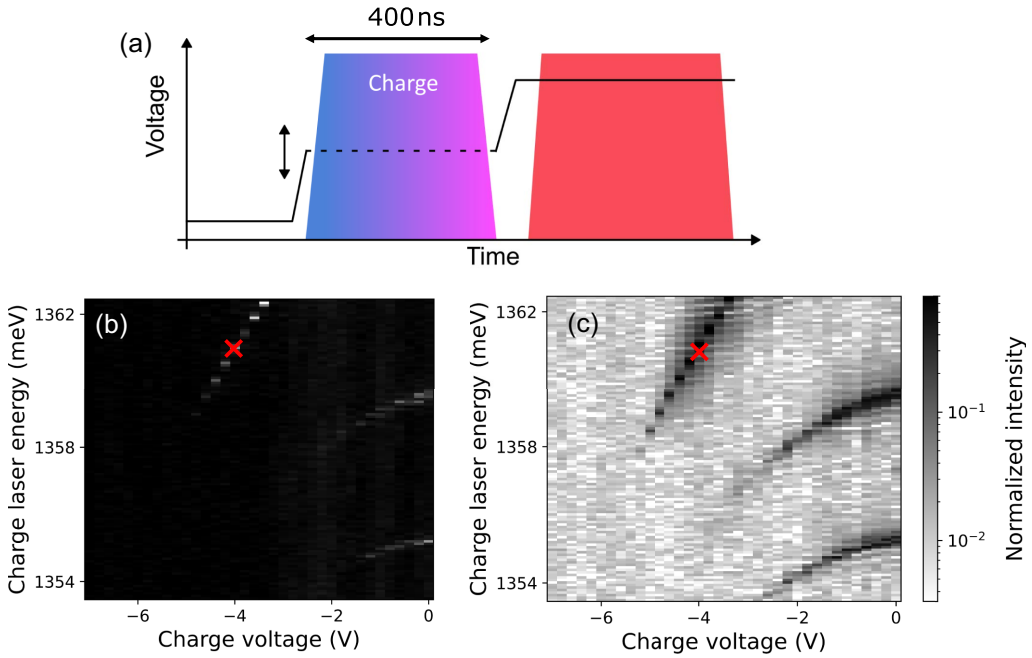

FIG. 12. (a) Experimental cycle used to determine the charging parameters for one-electron-charging. (b) X^0 intensity map as a function of charge voltage and charge laser energy. The cross marks the working point used for subsequent experiments in this manuscript. (c) X^- intensity map as a function of charge voltage and charge laser energy.

electron, we use a sequential charging method, where we keep the charge laser energy constant but vary the charge voltage. We found the optimal voltage to charge a second electron to be at −0.88 V.

In this section, we explain how we found these parameters. In a first step, we determine the optimal charge laser energy and charge voltage. For this, we employ the measurement cycle shown in Fig. 12(a), where the readout laser is set resonant with X^0 and the length of the charging sequence is 400 ns. As a readout voltage we typically choose 0.56 V since in this regime all three charged complexes under investigation are reasonably close together, yet still well distinguishable [see also Fig. 1(b)]. We then scan the two-dimensional parameter space by changing the charge laser energy [indicated by the color gradient of the laser pulse in Fig. 12(a)] and the charge laser voltage [indicated by the arrows next to the charge voltage level in Fig. 12(a)]. If no charging takes place, there will be a strong X^0 signal visible during the readout. However, if charging takes place, this signal should quench, since the readout laser is not resonant with the X^-. In Fig. 12(b), we observe that for most combinations of charge laser energy and charge voltage, the X^0 remains bright. But there are some valleys where the X^0 goes dark, which could be indicative of charging taking place.

To show that this is actual charging with one electron, we perform the same experiment, but with readout of X^-. The results of these measurements are shown in Fig. 12(c). One can see that the X^- turns bright exactly where the X^0 goes dark. This is a clear sign that the observed loss of the X^0 signal is due to one-electron charging.

As a working point for one-electron charging we chose −4 V as charging voltage and 1361.0 meV for the charge laser energy [marked as red crosses in Fig. 12(b) and 12(c)]. For two-electron charging, we keep the charge laser on at the same energy, but we vary the charge voltage so that the charge laser is resonant with an X^- transition. This will excite a trion, of which the hole tunnels out and the QDM is left with two electrons. To find the second charge voltage, we perform a similar experiment as before, but now we keep the charge laser energy fixed and only sweep the second charge voltage. The experimental cycle is shown in Fig. 13(a). The 400 ns charging sequence is now split into two 200 ns sequences, wherein the first 200 ns the first electron is charged at the voltage determined before for a laser of energy 1361.0 meV, i.e. −4.0 V. The same laser is gated on for charging the second electron (i.e. sequential charging) and the gate voltage is varied for the second charging step. Furthermore, we set the readout laser resonant with the X^{2-} transition to probe two-electron occupation. The result of this measurement is shown in Fig. 13(b). We observe a peak in the X^{2-} emission at around −0.88 V. We used this voltage to charge the QDM with a second electron for all experiments involving two electrons.

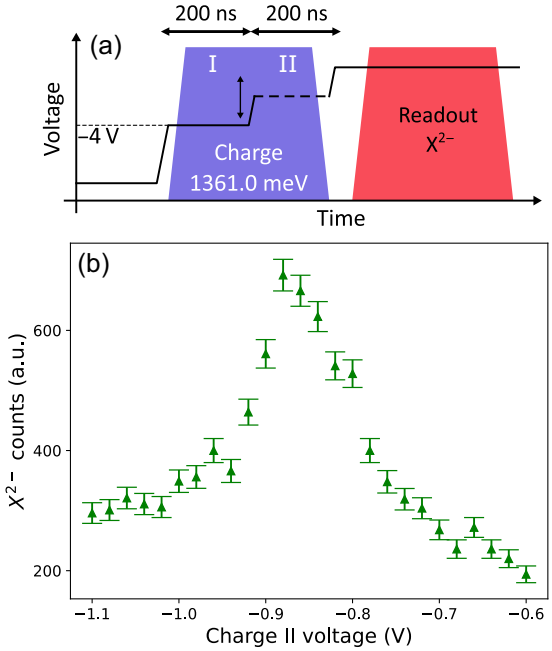

FIG. 13. (a) Experimental cycle used to charge the voltage for charging the second electron in the sequential charging scheme. (b) X^{2-} intensity vs second charge voltage plateau with the charge laser energy fixed at 1361.0 meV.

APPENDIX E: ESTIMATING CHARGING FIDELITIES

To estimate the charge fidelities, we follow the method in Ref. [25]. We denote the probability to charge n electrons given that m electrons were intended to be charged (i.e. the m is the number of charge plateaus) as $p(n|m)$. Our starting point is the assumption that the QDM is initialized (during the reset phase) to be perfectly empty, i.e. $p(0|0) = 1$. We furthermore restrict our analysis to the lowest three charge states X^0, X^- and X^{2-}. We denote the number of counts of charge state $a \in \{0, -, 2-\}$ given that $b \in \{0, 1, 2\}$ charge pulses were applied as N_b^a.

Now, the probability of charging one electron given that one pulse was applied is $p(1|1) = p(\neg 0|1) - p(2|1)$ where the probability of charging more than one electron given that one charge pulse was applied is

$$p(\neg 0|1) = \frac{N_0^0 - N_1^0}{N_0^0} \tag{E1}$$

and $p(2|1) \leq \frac{N_1^{2-}}{N_2^{2-}}$. Thus, the one-electron charging fidelity can be written as:

$$p(1|1) \geq \frac{N_0^0 - N_1^0}{N_0^0} - \frac{N_1^{2-}}{N_2^{2-}}. \tag{E2}$$

Using the count numbers from the sequential charging experiment presented in Sec. III, we determine a value of $p(1|1) \geq 85.9(\pm 0.2)\%$ from Eq. (E2). For the two-electron charging fidelity we can use $p(2|2) = 1 - p(1|2) - p(0|2)$ where $p(0|2) \leq 1 - p(\neg 0|1)$ and $p(1|2) \leq \frac{N_2^{2-}}{N_1^-}$. We arrive at the following expression for the two-electron charging fidelity:

$$p(2|2) \geq \frac{N_0^0 - N_1^0}{N_0^0} - \frac{N_2^-}{N_1^-}. \tag{E3}$$

We find $p(2|2) \geq 89.2(\pm 11.1)\%$ for our measured data.

APPENDIX F: SELECTION RULES OF THE DOUBLY CHARGED EXCITON

In this section, we derive the selection rules between the two-electron states and the doubly charged exciton states. While the selection rules in the (1, 1)-regime with applied magnetic field in growth direction, as presented in Fig. 3(d), can be understood intuitively from the change of the net spin in the upper dot [19,21], the selection rules in the (2, 0)-regime, where most experiments in Sec. VI were performed and are more complicated. Here, the doubly charged exciton state in terms of charge occupation is described by

$$\begin{pmatrix} 2 & 1 \\ 0 & 1 \end{pmatrix}. \tag{F1}$$

The state consists of an electron pair in the lower dot and an electron-hole pair in the upper dot. With regard to spin, this charged complex should therefore behave like a neutral exciton confined in the upper dot, and therefore the electron-hole-exchange interaction becomes an important factor that governs the selection rules for both the direct and indirect transition [52].

We base our theoretical calculation of the selection rules on the description in second quantization using the single electron states $|\psi_i\rangle$, where $i = \{\lambda_i, \alpha_i, \sigma_i\}$ is a compound quantum number describing the QD location $\alpha_i = (l, u)$ (for lower and upper QD), the band index $\lambda_i = (e, h)$ (for electrons and holes) and the spin $\sigma_i = (\uparrow, \downarrow)$. The light-matter interaction Hamiltonian, which governs the selection rules, is given by

$$H_{\mathrm{LM}} = -\boldsymbol{d} \cdot \boldsymbol{E}(\boldsymbol{r_0}, t) \tag{F2}$$

in the dipole approximation. $\boldsymbol{d} = -e\boldsymbol{r}$ is the dipole operator (with elementary charge e and position operator $\boldsymbol{r}$) and $\boldsymbol{E}(\boldsymbol{r_0}, t)$ is the time-dependent electric field at the emitter position $\boldsymbol{r_0}$. A monochromatic electric field of frequency ω can be decomposed into

$$\boldsymbol{E}(\boldsymbol{r_0}, t) \equiv \boldsymbol{E}^{(+)} \mathrm{e}^{-\mathrm{i}\omega t} + \boldsymbol{E}^{(-)} \mathrm{e}^{\mathrm{i}\omega t} \tag{F3}$$

with $\boldsymbol{E}^{(+)}$ ($\boldsymbol{E}^{(-)}$) being the positive (negative) frequency part of the electric field, which are the complex conjugates

of each other. In the rotating wave approximation and second quantization, the Hamiltonian can be rewritten into

$$H_{\mathrm{LM}} = -\sum_k E_k^{(+)} \sum_{i,j} \langle \psi_i | d^k | \psi_j \rangle e_i^\dagger h_j^\dagger + \mathrm{h.c.}. \tag{F4}$$

$E_k^{(+)} = \boldsymbol{E}^{(+)} \cdot \boldsymbol{e}_k$ is the projection of the positive-frequency electric field onto the k-th polarization basis vector and $d^k = \boldsymbol{d} \cdot \boldsymbol{e}_k^*$, where e_i (h_j) is the annihilation operator of an electron (a hole) in state $|\psi_i\rangle$ ($|\psi_j\rangle$) and the sum over i (j) only runs over electron (hole) states.

To calculate the many-body matrix elements, we need the single-particle dipole matrix elements $\langle \psi_i | d^k | \psi_j \rangle$. In the envelope function approximation, the wave functions are written as a product of the Bloch factor $u_{\lambda_i,\sigma_i}(\boldsymbol{r})$ and a slowly varying envelope function $\varphi_{\alpha_i}(\boldsymbol{r})$ [53,54]:

$$\psi_i(\boldsymbol{r}) = u_{\lambda_i,\sigma_i}(\boldsymbol{r}) \varphi_{\alpha_i}(\boldsymbol{r}). \tag{F5}$$

Then, the dipole matrix elements can be approximated as:

$$\begin{aligned} \langle \psi_i | d^k | \psi_j \rangle \approx & \int \mathrm{d}^3 r \, u^*_{\lambda_i,\sigma_i}(\boldsymbol{r}) d^k u_{\lambda_j,\sigma_j}(\boldsymbol{r}) \\ & \times \int \mathrm{d}^3 r \, \varphi^*_{\alpha_i}(\boldsymbol{r}) \varphi_{\alpha_j}(\boldsymbol{r}), \end{aligned} \tag{F6}$$

meaning that the selection rules are governed by the bulk dipole matrix elements, and the envelope functions only influence the amplitude of the transition. The spin-dependence of the Bloch factors is due to spin-orbit coupling. In InGaAs, the spin and orbital angular momentum of heavy holes are aligned. The hole Bloch factors have p-type symmetry (angular momentum $l = 1$) and we neglect light holes (non-aligned spin and orbital angular momentum), since they are higher in energy. The conduction band electrons have s-type symmetry ($l = 0$) and therefore do not exhibit direct spin-orbit coupling [52,55]. For circularly polarized light ($\boldsymbol{e}_{\sigma^+} = \frac{1}{\sqrt{2}}(1, \mathrm{i})^T$, $\boldsymbol{e}_{\sigma^-} = \frac{1}{\sqrt{2}}(1, -\mathrm{i})^T$), the matrix element selection rules can be inferred from symmetry considerations or by evaluating the angular part of the first integral in Eq. (F6). The only non-vanishing single-particle matrix elements are

$$\begin{aligned} \langle \psi_{\mathrm{e},\alpha,\downarrow} | d^{\sigma^+} | \psi_{\mathrm{h},\beta,\uparrow} \rangle &= \langle \psi_{\mathrm{e},\alpha,\uparrow} | d^{\sigma^-} | \psi_{\mathrm{h},\beta,\downarrow} \rangle \\ &\equiv D_{\alpha,\beta} \\ &= D^{(0)} \chi_{\alpha,\beta}. \end{aligned} \tag{F7}$$

Their amplitudes are given by the bulk dipole matrix element $D^{(0)}$ and the envelope function overlap $\chi_{\alpha,\beta} = \int \mathrm{d}^3 r \, \varphi^*_\alpha(\boldsymbol{r}) \varphi_\beta(\boldsymbol{r})$. Therefore, direct transitions ($\alpha = \beta$) do have stronger transition amplitudes than indirect ($\alpha \neq \beta$) ones. To calculate the transition amplitudes, we first define all relevant states in terms of creation operators. We consider all two-electron states

$$\begin{aligned} |S_0\rangle &= \frac{1}{\sqrt{2}} (e^\dagger_{l,\uparrow} e^\dagger_{u,\downarrow} - e^\dagger_{l,\downarrow} e^\dagger_{u,\uparrow}) |\mathrm{vac}\rangle, \\ |T_0\rangle &= \frac{1}{\sqrt{2}} (e^\dagger_{l,\uparrow} e^\dagger_{u,\downarrow} + e^\dagger_{l,\downarrow} e^\dagger_{u,\uparrow}) |\mathrm{vac}\rangle, \\ |S_u\rangle &= e^\dagger_{u,\uparrow} e^\dagger_{u,\downarrow} |\mathrm{vac}\rangle, \\ |S_l\rangle &= e^\dagger_{l,\uparrow} e^\dagger_{l,\downarrow} |\mathrm{vac}\rangle, \\ |T_-\rangle &= e^\dagger_{l,\downarrow} e^\dagger_{u,\downarrow} |\mathrm{vac}\rangle, \\ |T_+\rangle &= e^\dagger_{l,\uparrow} e^\dagger_{u,\uparrow} |\mathrm{vac}\rangle. \end{aligned} \tag{F8}$$

For the doubly charged exciton states, we will only focus on the aforementioned $\left(\begin{smallmatrix} 2 & 1 \\ 0 & 1 \end{smallmatrix}\right)$-states, for which we will introduce the shorthand notation $|Q\rangle$. With electron-hole-exchange interaction of the exciton in the upper dot included, the eigenstates at zero magnetic field can be expressed in terms of creation operators as:

$$\begin{aligned} |Q_{1\pm}\rangle &= \frac{1}{\sqrt{2}} e^\dagger_{l,\uparrow} e^\dagger_{l,\downarrow} (e^\dagger_{u,\downarrow} h^\dagger_{u,\uparrow} \pm e^\dagger_{u,\uparrow} h^\dagger_{u,\downarrow}) |\mathrm{vac}\rangle, \\ |Q_{2\pm}\rangle &= \frac{1}{\sqrt{2}} e^\dagger_{l,\uparrow} e^\dagger_{l,\downarrow} (e^\dagger_{u,\uparrow} h^\dagger_{u,\uparrow} \pm e^\dagger_{u,\downarrow} h^\dagger_{u,\downarrow}) |\mathrm{vac}\rangle. \end{aligned} \tag{F9}$$

The eigenstates are two well-known bright states with total spin projection $M = 1\pm$ and two dark states with total spin projection $M = 2\pm$.

Now, we consider the basis given in Eq. (F8) and the last four states in Eq. (F9) in that order. The dipole Hamiltonian in this basis is given by

$$\begin{aligned} H_{\mathrm{LM}} = & E^{(+)}_{\sigma^+} \left[\frac{d_{lu}}{2} (|Q_{1+}\rangle\langle S_0| + |Q_{1+}\rangle\langle T_0| + |Q_{1-}\rangle\langle S_0| + |Q_{1-}\rangle\langle T_0|) \right. \\ & \left. + \frac{d_{uu}}{\sqrt{2}} (|Q_{1+}\rangle\langle S_l| + |Q_{1-}\rangle\langle S_l|) + \frac{d_{lu}}{\sqrt{2}} (|Q_{2+}\rangle\langle T_+| + |Q_{2-}\rangle\langle T_+|) \right] \\ & + E^{(+)}_{\sigma^-} \left[\frac{d_{lu}}{2} (-|Q_{1+}\rangle\langle S_0| + |Q_{1+}\rangle\langle T_0| + |Q_{1-}\rangle\langle S_0| - |Q_{1-}\rangle\langle T_0|) \right. \\ & \left. + \frac{d_{uu}}{\sqrt{2}} (|Q_{1+}\rangle\langle S_l| - |Q_{1-}\rangle\langle S_l|) + \frac{d_{lu}}{\sqrt{2}} (|Q_{2+}\rangle\langle T_+| - |Q_{2-}\rangle\langle T_+|) \right] + \mathrm{h.c.} \end{aligned} \tag{F10}$$

which can be transformed into the linear representation:

$$H_{\mathrm{LM}} = E_{\mathrm{h}}^{(+)}\left[\frac{d_{lu}}{\sqrt{2}}(|Q_{1+}\rangle\langle T_0| + |Q_{1-}\rangle\langle S_0|) + d_{uu}|Q_{1+}\rangle\langle S_l| + \frac{d_{lu}}{2}(|Q_{2+}\rangle\langle T_-| + |Q_{2+}\rangle\langle T_+| - |Q_{2-}\rangle\langle T_-| + |Q_{2-}\rangle\langle T_+|)\right] - \mathrm{i}E_{\mathrm{v}}^{(+)}\left[\frac{d_{lu}}{\sqrt{2}}(|Q_{1+}\rangle\langle S_0| + |Q_{1-}\rangle\langle T_0|) + d_{uu}|Q_{1-}\rangle\langle S_l| + \frac{d_{lu}}{2}(-|Q_{2+}\rangle\langle T_-| + |Q_{2+}\rangle\langle T_+| + |Q_{2-}\rangle\langle T_-| + |Q_{2-}\rangle\langle T_+|)\right] + \mathrm{h.c.} \quad \text{(F11)}$$

by using

$$E_{\mathrm{h}} = \frac{1}{\sqrt{2}}(E_{\sigma^+} + E_{\sigma^-}), \quad E_{\mathrm{v}} = \frac{\mathrm{i}}{\sqrt{2}}(E_{\sigma^+} - E_{\sigma^-}). \quad \text{(F12)}$$

The selection rules that can be inferred from this Hamiltonian are displayed as a level scheme in Fig. 14. The states $|Q_{1\pm}\rangle$ couple to $|S_0\rangle$, $|T_0\rangle$ and $|S_l\rangle$ via linearly polarized photons, while $|Q_{2\pm}\rangle$ each couples to the remaining triplet states via circularly polarized photons. This leads to the formation of two subspaces that do not couple optically.

In our experiments we optically drive the transition $|S_l\rangle \leftrightarrow |Q_{1-}\rangle$ with a narrow band cw-laser, such that the other trion states can be safely neglected.

The scheme of $|T_0\rangle$-pumping is shown Fig. 15. With the state initialized into the $|S_l\rangle$ state, it is pumped into the $|Q_{1-}\rangle$ state via linearly polarized light. From there, $|Q_{1-}\rangle$ can decay back into $|S_l\rangle$, which is however offset by the continuous pumping. A portion of the population decays into both $|S_0\rangle$ and $|T_0\rangle$ with roughly equal rate γ_{lu}. The delocalized singlet $|S_0\rangle$ quickly decays back into $|S_l\rangle$ due to phonon-assisted tunneling (γ_{phon}) on the order of picoseconds, similar to fast interdot tunneling of a single electron, and is re-excited by the pump laser. The population in $|T_0\rangle$ stays there for a longer time since phonon-assisted tunneling preserves spin and therefore only allows transitions between singlet and triplet states due to small contributions stemming from Dresselhaus spin-orbit coupling and other spin-flip processes, which are however much slower [40,56].

It should be noted that this simple analytic derivation does not take into account various aspects of the actual quantum dot molecule, such as lateral misalignment of the dots, different lateral asymmetry of the two dots, heavy-light-hole mixing and different strain environments in each dot, all of which are expected to slightly change the idealized selection rules shown in Fig. 14 [19,57].

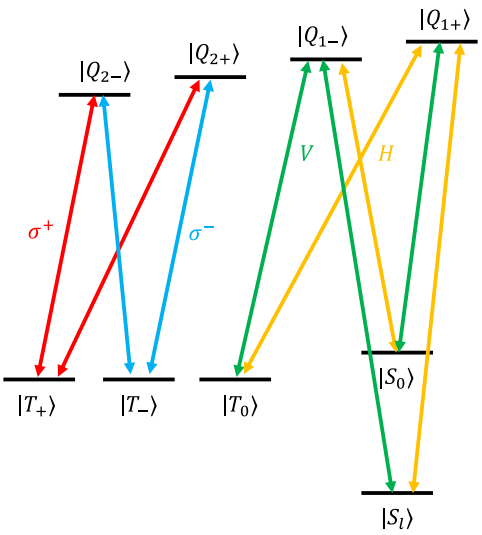

FIG. 14. Level scheme and optical transitions between $|Q\rangle$ states and the two-electron states. Linearly polarized transitions are displayed in green (vertical) and yellow (horizontal), while circularly polarized transitions are displayed in red (σ^+) and blue (σ^-).

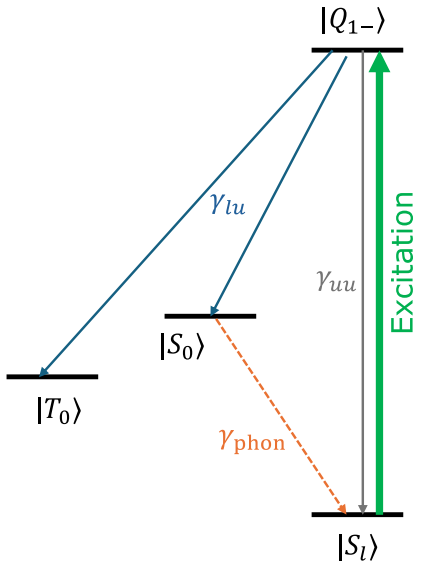

FIG. 15. Level scheme for the $2e$ pumping of the $|T_0\rangle$ state.

APPENDIX G: THE PHONON-DRIVEN QUANTUM KINETICS OF THE SINGLET-TRIPLET CONFIGURATIONS

In this section, we consider the triplet T_0 to the singlet S phonon-assisted transitions. The modeling is based on the eight-band $\boldsymbol{k}\cdot\boldsymbol{p}$ theory and involves structural calculations in the real space.

1. The structural calculations

The shapes of the quantum dots are modeled using truncated Gaussian profiles [44]. The top surface of each dot is described by

$$S(x,y)=\min\left(w\,\exp\left[-\frac{x^2+y^2}{2d^2}\right],h\right),$$

where h denotes the dot height, d controls the lateral size, and w sets the Gaussian steepness. For the lower and upper dots (indexed by l and u), the parameters are $h_l=3.5a$, $d_l=48a$, $w_l=25a$, and $h_u=4a$, $d_u=52a$, $w_u=25a$, with a being the lattice constant. Both dots are placed on wetting layers of thickness a. The separation between the dots (base to base) is $17.5a$, and the $Al_{0.33}Ga_{0.67}As$ barrier between them has a thickness of $4.5a$.

To describe the individual QD morphology, we employ the trumpet-shaped composition profile [58,59], in which the local indium concentration inside the quantum dots is described by

$$C(\boldsymbol{r})=C_l+(C_u-C_l)\exp\left\{-\frac{\sqrt{x^2+y^2}\exp -z/z_0}{r_0}\right\}.$$

Here, C_u and C_l denote the maximum and minimum indium contents in the QD, respectively, while r_0 and z_0 determine the spatial extent of the profile. For both quantum dots, we set $C_u=0.42$ ($In_{0.42}Ga_{0.58}As$), $C_l=0.3$ ($In_{0.3}Ga_{0.7}As$), and $r_0=20a$. The vertical decay parameters were chosen as $z_{0l}=3.5a$ for the lower dot and $z_{0u}=4.0a$ for the upper one. The dots are separated by the distance $D=17.5a$. The cross section of the resulting material distribution is shown in Fig. 16.

The strain caused by the lattice mismatch between the involved materials is taken into account within the continuous elasticity approach [60] with the parameters from Vurgaftman *et al.* [61]. As in the zinc-blende structure shear strain comes with a piezoelectric field; we accounted for this effect with polarization up the second order in the strain tensor components [62]. Here, we took the parameters from Caro *et al.* [63].

2. The energy levels

The wave functions for the electron single-particle states are found within the eight-band $\boldsymbol{k}\cdot\boldsymbol{p}$ model in the envelope function approximation, as described in Refs. [43,44]. To account for the gate electric field effect, the real-space Hamiltonian is supplemented by the diagonal term:

$$V_F=eF(z-z_c),$$

where z_c is between QDs. For $F\leq 17$ kV/cm, we calculate 12 states: six energetically lowest states (the s and p-type envelope) in the lower QD and the corresponding six states of the upper QD. For larger fields, we take the 6 and 2 lowest states in the lower and in the upper QD, respectively, which is motivated by better numerical stability. Therefore, the 12 (or 8) states form a basis for the configuration interaction procedure, which is the next stage of our modeling.

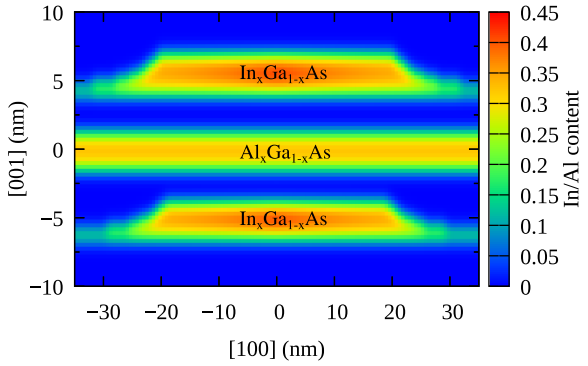

FIG. 16. The indium distribution ($In_xGa_{1-x}As$) in the QDs and Al content ($Al_xGa_{1-x}As$) in the barrier.

The two-electron states are found from the diagonalization of the Coulomb Hamiltonian using the configuration interaction method. The calculated energy levels are shown in Fig. 6(c). The simulations were carried out at a small magnetic field $B=0.1$ T in the Faraday orientation, which was chosen rather arbitrarily for illustrative purposes. As can be seen, the obtained singlet-triplet energy splitting at the sweet spot (here around $F\approx 10$ kV/cm) of 870 μeV is reasonably close to the experimental value (718 μeV). The character of states in the vicinity of the sweet spot was discussed in the main part of the text. Here, we focus on the configurations at higher electric fields (e.g. $F\approx 22$ kV/cm), which favor the localization in the lower dot. In this regime, the lowest state is the spin singlet localized in the lower QD $|S_l\rangle$. The next two branches are the triplet states $|T'_{-/0/+}\rangle$ and $|T''_{-/0/+}\rangle$, build on the s and p shell states in the lower QD. The next states are the s-shell triplet $|T_{-/0/+}\rangle$ and the singlet $|S_0\rangle$. The other upper branches are the singlet configurations involving s- and p-shell in the lower QD, but they will not be taken into account in this analysis. To describe the states of interest, we introduce an extended notation, accounting for the orbital type:

$$
\begin{aligned}
|S_l\rangle &= e^{\dagger}_{l(s),\uparrow} e^{\dagger}_{l(s),\downarrow}|\mathrm{vac}\rangle,\\
|T_-\rangle &= e^{\dagger}_{l(s),\downarrow} e^{\dagger}_{u(s),\downarrow}|\mathrm{vac}\rangle\\
|T_0\rangle &= \frac{1}{\sqrt{2}}(e^{\dagger}_{l(s),\uparrow} e^{\dagger}_{u(s),\downarrow} + e^{\dagger}_{l(s),\downarrow} e^{\dagger}_{u(s),\uparrow})|\mathrm{vac}\rangle,\\
|T_+\rangle &= e^{\dagger}_{l(s),\uparrow} e^{\dagger}_{u(s),\uparrow}|\mathrm{vac}\rangle,\\
|T'_-\rangle &= e^{\dagger}_{l(s),\downarrow} e^{\dagger}_{l(p_1),\downarrow}|\mathrm{vac}\rangle,\\
|T'_0\rangle &= \frac{1}{\sqrt{2}}(e^{\dagger}_{l(s),\uparrow} e^{\dagger}_{l(p_1),\downarrow} + e^{\dagger}_{l(s),\downarrow} e^{\dagger}_{l(p_1),\uparrow})|\mathrm{vac}\rangle,\\
|T'_+\rangle &= e^{\dagger}_{l(s),\uparrow} e^{\dagger}_{l(p_1),\uparrow}|\mathrm{vac}\rangle,\\
|T''_-\rangle &= e^{\dagger}_{l(s),\downarrow} e^{\dagger}_{l(p_2),\downarrow}|\mathrm{vac}\rangle,\\
|T''_0\rangle &= \frac{1}{\sqrt{2}}(e^{\dagger}_{l(s),\uparrow} e^{\dagger}_{l(p_2),\downarrow} + e^{\dagger}_{l(s),\downarrow} e^{\dagger}_{l(p_2),\uparrow})|\mathrm{vac}\rangle,\\
|T''_+\rangle &= e^{\dagger}_{l(s),\uparrow} e^{\dagger}_{l(p_2),\uparrow}|\mathrm{vac}\rangle,\\
|S_0\rangle &= \frac{1}{\sqrt{2}}(e^{\dagger}_{l(s),\uparrow} e^{\dagger}_{u(s),\downarrow} - e^{\dagger}_{l(s),\downarrow} e^{\dagger}_{u(s),\uparrow})|\mathrm{vac}\rangle, \qquad \text{(G1)}
\end{aligned}
$$

where $e^{\dagger}_{l(\alpha),\uparrow/\downarrow}$ ($e^{\dagger}_{u(\alpha),\uparrow/\downarrow}$) is the creation operator of the α-th electron orbital state with $\uparrow/\downarrow$ spin in the lower (upper) dot.

3. Phonon-assisted transitions

We calculated phonon-assisted relaxation rates between the two-electron energy levels within Fermi's golden rule:

$$
\gamma_{\mathrm{phon}}(i \to j) = \frac{2\pi}{\hbar}\sum_{\boldsymbol{k},\lambda}|G_{ij,\lambda}(\boldsymbol{k})|^2 \times [\delta(\Delta E_{ij} - \hbar c_\lambda k) + \delta(\Delta E_{ij} + \hbar c_\lambda k)],
$$

where $\Delta E_{ij} = E_i - E_j$ is the energy difference between the energy levels, $G_{ij,\lambda}(\boldsymbol{k})$ is the two-electron form factor, as described in Ref. [40]; λ is the phonon branch (two transversal and a longitudinal one), and c_λ is the speed of sound. Here, we take into account the coupling between the electrons and phonons via the deformation potential and the piezoelectric field [46–48]. The material parameters used in calculations are listed in the Appendix of Ref. [44]. Here, we consider the zero-temperature case, i.e. the transitions from the energetically upper to the lower states (phonon emission). We also note that we take into account only the spin-flip transitions due to the spin-orbit interaction, neglecting the hyperfine-coupling-related effects. While hyperfine- and spin-orbit-induced spin relaxation originate from different couplings, both mechanisms interact with the same phonon bath and thus share the same phonon spectral density. Consequently, the present model provides an insight into phonon-related transitions, even though the absolute relaxation rates for the two mechanisms may differ substantially.

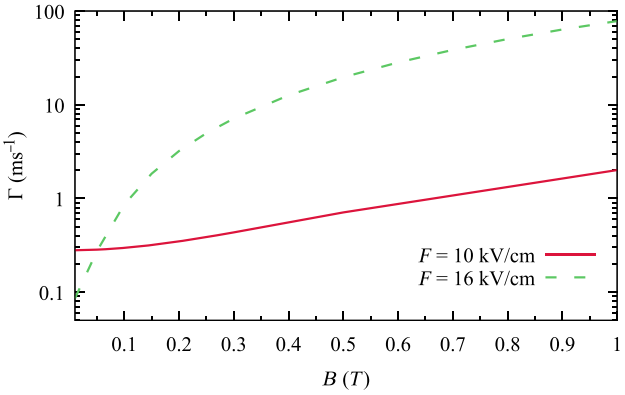

FIG. 17. The magnetic-field dependence of the $|T_0\rangle \to |S\rangle$ phonon-assisted relaxation rate at two values of the electric field.

The calculated direct phonon-assisted transition rate between the T_0 and the lowest singlet state S is shown in Fig. 6(d). The electric field dependence and how it compares to the experimentally measured ones shown in Fig. 6(b) are discussed in Sec. VI of the main part of the text. We note that the spin-orbit-induced phonon-assisted transitions depend very strongly on the magnetic field. This dependence is illustrated in Fig. 17 for two representative electric field values: one close to the sweet spot ($F = 10$ kV/cm) and one near the maximum of the $|T_0\rangle \to |S\rangle$ transition rate ($F \approx 16$ kV/cm). In the latter case, the increase with magnetic field is much less pronounced, because the spin-orbit coupling mechanism associated with the difference between the g-factors of the two quantum dots is suppressed [40].

[1] D. D. Awschalom, R. Hanson, J. Wrachtrup, and B. B. Zhou, *Quantum technologies with optically interfaced solid-state spins*, Nat. Photonics **12**, 516 (2018).

[2] L. Hanschke, K. A. Fischer, S. Appel, D. Lukin, J. Wierzbowski, S. Sun, R. Trivedi, J. Vučković, J. J. Finley, and K. Müller, *Quantum dot single-photon sources with ultra-low multi-photon probability*, npj Quantum Inf. **4**, 43 (2018).

[3] S. Thomas, M. Billard, N. Coste, S. Wein, H. Ollivier, O. Krebs, L. Tazaïrt, A. Harouri, A. Lemaitre, I. Sagnes, C. Anton, L. Lanco, N. Somaschi, J. Loredo, and P. Senellart, *Bright polarized single-photon source based on a linear dipole*, Phys. Rev. Lett. **126**, 233601 (2021).

[4] N. Akopian, N. H. Lindner, E. Poem, Y. Berlatzky, J. Avron, D. Gershoni, B. D. Gerardot, and P. M. Petroff, *Entangled photon pairs from semiconductor quantum dots*, Phys. Rev. Lett. **96**, 130501 (2006).

[5] D. Press, T. D. Ladd, B. Zhang, and Y. Yamamoto, *Complete quantum control of a single quantum dot spin using ultrafast optical pulses*, Nature (London) **456**, 218 (2008).

[6] W. B. Gao, P. Fallahi, E. Togan, J. Miguel-Sanchez, and A. Imamoglu, *Observation of entanglement between a*

quantum dot spin and a single photon, Nature (London) **491**, 426 (2012).

[7] R. Stockill, M. Stanley, L. Huthmacher, E. Clarke, M. J. Hugues, A. J. Miller, C. Matthiesen, C. Le Gall, and M. Atatüre, *Phase-tuned entangled state generation between distant spin qubits*, Phys. Rev. Lett. **119**, 010503 (2017).

[8] N. H. Lindner and T. Rudolph, *Proposal for pulsed on-demand sources of photonic cluster state strings*, Phys. Rev. Lett. **103**, 113602 (2009).

[9] I. Schwartz, E. Schmidgall, L. Gantz, D. Cogan, E. Bordo, Y. Don, M. Zielinski, and D. Gershoni, *Deterministic writing and control of the dark exciton spin using short single optical pulses*, Phys. Rev. X **5**, 011009 (2015).

[10] D. Cogan, Z.-E. Su, O. Kenneth, and D. Gershoni, *Deterministic generation of indistinguishable photons in a cluster state*, Nat. Photonics **17**, 324 (2023).

[11] N. Coste, D. A. Fioretto, N. Belabas, S. C. Wein, P. Hilaire, R. Frantzeskakis, M. Gundin, B. Goes, N. Somaschi, M. Morassi, A. Lemaître, I. Sagnes, A. Harouri, S. E. Economou, A. Auffeves, O. Krebs, L. Lanco, and P. Senellart, *High-rate entanglement between a semiconductor spin and indistinguishable photons*, Nat. Photonics **17**, 582 (2023).

[12] R. Raussendorf, D. E. Browne, and H. J. Briegel, *Measurement-based quantum computation on cluster states*, Phys. Rev. A **68**, 022312 (2003).

[13] D. E. Browne and T. Rudolph, *Resource-efficient linear optical quantum computation*, Phys. Rev. Lett. **95**, 010501 (2005).

[14] S. E. Economou, N. Lindner, and T. Rudolph, *Optically generated 2-dimensional photonic cluster state from coupled quantum dots*, Phys. Rev. Lett. **105**, 093601 (2010).

[15] M. Gimeno-Segovia, T. Rudolph, and S. E. Economou, *Deterministic generation of large-scale entangled photonic cluster state from interacting solid state emitters*, Phys. Rev. Lett. **123**, 070501 (2019).

[16] H. J. Krenner, M. Sabathil, E. C. Clark, A. Kress, D. Schuh, M. Bichler, G. Abstreiter, and J. J. Finley, *Direct observation of controlled coupling in an individual quantum dot molecule*, Phys. Rev. Lett. **94**, 057402 (2005).

[17] M. F. Doty, M. Scheibner, A. S. Bracker, I. V. Ponomarev, T. L. Reinecke, and D. Gammon, *Optical spectra of doubly charged quantum dot molecules in electric and magnetic fields*, Phys. Rev. B **78**, 115316 (2008).

[18] H. Bluhm, S. Foletti, I. Neder, M. Rudner, D. Mahalu, V. Umansky, and A. Yacoby, *Dephasing time of GaAs electron-spin qubits coupled to a nuclear bath exceeding* 200 μs, Nat. Phys. **7**, 109 (2011).

[19] K. M. Weiss, J. M. Elzerman, Y. L. Delley, J. Miguel-Sanchez, and A. Imamoğlu, *Coherent two-electron spin qubits in an optically active pair of coupled* InGaAs *quantum dots*, Phys. Rev. Lett. **109**, 107401 (2012).

[20] K. X. Tran, A. S. Bracker, M. K. Yakes, J. Q. Grim, and S. G. Carter, *Enhanced spin coherence of a self-assembled quantum dot molecule at the optimal electrical bias*, Phys. Rev. Lett. **129**, 027403 (2022).

[21] Y. L. Delley, M. Kroner, S. Faelt, W. Wegscheider, and A. İmamoğlu, *Deterministic entanglement between a propagating photon and a singlet-triplet qubit in an optically active quantum dot molecule*, Phys. Rev. B **96**, 241410 (2017).

[22] S. E. Economou and T. L. Reinecke, *Optically induced spin gates in coupled quantum dots using the electron-hole exchange interaction*, Phys. Rev. B **78**, 115306 (2008).

[23] D. Kim, S. G. Carter, A. Greilich, A. S. Bracker, and D. Gammon, *Ultrafast optical control of entanglement between two quantum-dot spins*, Nat. Phys. **7**, 223 (2011).

[24] A. Greilich, S. G. Carter, D. Kim, A. S. Bracker, and D. Gammon, *Optical control of one and two hole spins in interacting quantum dots*, Nat. Photonics **5**, 702 (2011).

[25] F. Bopp, J. Rojas, N. Revenga, H. Riedl, F. Sbresny, K. Boos, T. Simmet, A. Ahmadi, D. Gershoni, J. Kasprzak, A. Ludwig, S. Reitzenstein, A. Wieck, D. Reuter, K. Müller, and J. J. Finley, *Quantum dot molecule devices with optical control of charge status and electronic control of coupling*, Adv. Quantum Technol. **5**, 2200049 (2022).

[26] F. Bopp, J. Schall, N. Bart, F. Vögl, C. Cullip, F. Sbresny, K. Boos, C. Thalacker, M. Lienhart, S. Rodt, D. Reuter, A. Ludwig, A. D. Wieck, S. Reitzenstein, K. Müller, and J. J. Finley, *Coherent driving of direct and indirect excitons in a quantum dot molecule*, Phys. Rev. B **107**, 165426 (2023).

[27] I. Schwartz, D. Cogan, E. R. Schmidgall, Y. Don, L. Gantz, O. Kenneth, N. H. Lindner, and D. Gershoni, *Deterministic generation of a cluster state of entangled photons*, Science **354**, 434 (2016).

[28] S. Rodt and S. Reitzenstein, *High-performance deterministic in situ electron-beam lithography enabled by cathodoluminescence spectroscopy*, Nano Express **2**, 014007 (2021).

[29] J. Schall, M. Deconinck, N. Bart, M. Florian, M. von Helversen, C. Dangel, R. Schmidt, L. Bremer, F. Bopp, I. Hüllen, C. Gies, D. Reuter, A. D. Wieck, S. Rodt, J. J. Finley, F. Jahnke, A. Ludwig, and S. Reitzenstein, *Bright electrically controllable quantum-dot-molecule devices fabricated by in situ electron-beam lithography*, Adv. Quantum Technol. **4**, 2100002 (2021).

[30] M. Bayer, P. Hawrylak, K. Hinzer, S. Fafard, M. Korkusinski, Z. R. Wasilewski, O. Stern, and A. Forchel, *Coupling and entangling of quantum states in quantum dot molecules*, Science **291**, 451 (2001).

[31] R. J. Warburton, *Single spins in self-assembled quantum dots*, Nat. Mater. **12**, 483 (2013).

[32] A. Bechtold, D. Rauch, F. Li, T. Simmet, P.-L. Ardelt, A. Regler, K. Müller, N. A. Sinitsyn, and J. J. Finley, *Three-stage decoherence dynamics of an electron spin qubit in an optically active quantum dot*, Nat. Phys. **11**, 1005 (2015).

[33] J. R. Petta, A. C. Johnson, J. M. Taylor, E. A. Laird, A. Yacoby, M. D. Lukin, C. M. Marcus, M. P. Hanson, and A. C. Gossard, *Coherent manipulation of coupled electron spins in semiconductor quantum dots*, Science **309**, 2180 (2005).

[34] M. C. Löbl, C. Spinnler, A. Javadi, L. Zhai, G. N. Nguyen, J. Ritzmann, L. Midolo, P. Lodahl, A. D. Wieck, A. Ludwig, and R. J. Warburton, *Radiative Auger process in the single-photon limit*, Nature Nanotechnol. **15**, 558 (2020).

[35] A. Kurzmann, A. Ludwig, A. D. Wieck, A. Lorke, and M. Geller, *Auger recombination in self-assembled quantum*

dots: quenching and broadening of the charged exciton transition, Nano Lett. **16**, 3367 (2016).

[36] S. Wilksen, F. Lohof, I. Willmann, F. Bopp, M. Lienhart, C. Thalacker, J. Finley, M. Florian, and C. Gies, *Gate-based protocol simulations for quantum repeaters using quantum-dot molecules in switchable electric fields*, Adv. Quantum Technol. **7**, 2300280 (2024).

[37] M. Born and V. Fock, *Beweis des adiabatensatzes*, Zeitschrift für Physik **51**, 165 (1928).

[38] T. Kato, *On the adiabatic theorem of quantum mechanics*, J. Phys. Soc. Jpn. **5**, 435 (1950).

[39] K. Müller, A. Bechtold, C. Ruppert, M. Zecherle, G. Reithmaier, M. Bichler, H. J. Krenner, G. Abstreiter, A. W. Holleitner, J. M. Villas-Boas, M. Betz, and J. J. Finley, *Electrical control of inter-dot electron tunneling in a quantum dot molecule*, Phys. Rev. Lett. **108**, 197402 (2012).

[40] K. Gawarecki and P. Machnikowski, *Phonon-assisted relaxation between triplet and singlet states in a self-assembled double quantum dot*, Sci. Rep. **11**, 15256 (2021).

[41] A. V. Khaetskii and Y. V. Nazarov, *Spin relaxation in semiconductor quantum dots*, Phys. Rev. B **61**, 12639 (2000).

[42] A. V. Khaetskii and Y. V. Nazarov, *Spin-flip transitions between Zeeman sublevels in semiconductor quantum dots*, Phys. Rev. B **64**, 125316 (2001).

[43] K. Gawarecki, *Spin-orbit coupling and magnetic-field dependence of carrier states in a self-assembled quantum dot*, Phys. Rev. B **97**, 235408 (2018).

[44] M. Lienhart, K. Gawarecki, M. Stöcker, F. Bopp, C. Cullip, N. Akhlaq, C. Thalacker, J. Schall, S. Rodt, A. Ludwig, D. Reuter, S. Reitzenstein, K. Müller, P. Machnikowski, and J. J. Finley, *Resonant and antiresonant exciton-phonon coupling in quantum dot molecules*, Phys. Rev. B **112**, 235305 (2025).

[45] B. Urbaszek, X. Marie, T. Amand, O. Krebs, P. Voisin, P. Maletinsky, A. Högele, and A. Imamoglu, *Nuclear spin physics in quantum dots: An optical investigation*, Rev. Mod. Phys. **85**, 79 (2013).

[46] P. Y. Yu and M. Cardona, *Fundamentals of Semiconductors*, 3rd ed. (Springer, Berlin, 2005).

[47] A. Grodecka, L. Jacak, P. Machnikowski, and K. Roszak, *Phonon impact on the coherent control of quantum states in semiconductor quantum dots*, in *Quantum Dots: Research Developments*, edited by P. A. Ling (Nova Science, NY, 2005), pp. 47–88, cond-mat/0404364.

[48] M. Krzykowski, K. Gawarecki, and P. Machnikowski, *Hole spin-flip transitions in a self-assembled quantum dot*, Phys. Rev. B **102**, 205301 (2020).

[49] P. Karwat, K. Gawarecki, and P. Machnikowski, *Hole spin-flip transitions in a self-assembled quantum dot*, Phys. Rev. B **104**, 045308 (2021).

[50] S. Wijitpatima, N. Auler, P. Mudi, T. Funk, A. Barua, B. Shrestha, J. Schall, I. Limame, S. Rodt, D. Reuter, and S. Reitzenstein, *Bright electrically contacted circular Bragg grating resonators with deterministically integrated quantum dots*, ACS Nano **18**, 31834 (2024).

[51] M. Scheibner, M. F. Doty, I. V. Ponomarev, A. S. Bracker, E. A. Stinaff, V. L. Korenev, T. L. Reinecke, and D. Gammon, *Spin fine structure of optically excited quantum dot molecules*, Phys. Rev. B **75**, 245318 (2007).

[52] M. Bayer, G. Ortner, O. Stern, A. Kuther, A. A. Gorbunov, A. Forchel, P. Hawrylak, S. Fafard, K. Hinzer, T. L. Reinecke, S. N. Walck, J. P. Reithmaier, F. Klopf, and F. Schäfer, *Fine structure of neutral and charged excitons in self-assembled* In(Ga)As/(Al)GaAs *quantum dots*, Phys. Rev. B **65**, 195315 (2002).

[53] H. Haug and A.-P. Jauho, *Quantum Kinetics in Transport and Optics of Semiconductors* (Springer, New York, 2008).

[54] W. W. Chow and F. Jahnke, *On the physics of semiconductor quantum dots for applications in lasers and quantum optics*, Prog. Quantum Electron. **37**, 109 (2013).

[55] O. Gywat, H. J. Krenner, and J. Berezovsky, *Spins in Optically Active Quantum Dots: Concepts and Methods* (John Wiley & Sons, New York, 2010).

[56] M. Gawełczyk and K. Gawarecki, *Tunneling-related electron spin relaxation in self-assembled quantum-dot molecules*, Phys. Rev. B **103**, 245422 (2021).

[57] D. Farfurnik, R. M. Pettit, Z. Luo, and E. Waks, *Single-shot readout of a solid-state spin in a decoherence-free subspace*, Phys. Rev. Appl. **15**, L031002 (2021).

[58] V. Jovanov, T. Eissfeller, S. Kapfinger, E. C. Clark, F. Klotz, M. Bichler, J. G. Keizer, P. M. Koenraad, M. S. Brandt, G. Abstreiter, and J. J. Finley, *Highly nonlinear excitonic Zeeman spin splitting in composition-engineered artificial atoms*, Phys. Rev. B **85**, 165433 (2012).

[59] M. A. Migliorato, A. G. Cullis, M. Fearn, and J. H. Jefferson, *Atomistic simulation of strain relaxation in* $In_xGa_{1-x}As/GaAs$ *quantum dots with nonuniform composition*, Phys. Rev. B **65**, 115316 (2002).

[60] C. Pryor, J. Kim, L. W. Wang, A. J. Williamson, and A. Zunger, *Comparison of two methods for describing the strain profiles in quantum dots*, J. Appl. Phys. **83**, 2548 (1998).

[61] I. Vurgaftman, J. R. Meyer, and L. R. Ram-Mohan, *Band parameters for III–V compound semiconductors and their alloys*, J. Appl. Phys. **89**, 5815 (2001).

[62] G. Bester, X. Wu, D. Vanderbilt, and A. Zunger, *Importance of second-order piezoelectric effects in zinc-blende semiconductors*, Phys. Rev. Lett. **96**, 187602 (2006).

[63] M. A. Caro, S. Schulz, and E. P. O'Reilly, *Origin of nonlinear piezoelectricity in III-V semiconductors: Internal strain and bond ionicity from hybrid-functional density functional theory*, Phys. Rev. B **91**, 75203 (2015).